

X-ray scaling relations of early-type galaxies in IllustrisTNG and a new way of identifying backsplash objects

Yunchong Wang^{1,2*}, Mark Vogelsberger^{3,4}, Dong-Woo Kim⁵, Josh Borrow³, Aaron Smith⁵, Lars Hernquist⁵ and Wenjie Lin⁶

¹*Physics Department, Stanford University, 382 Via Pueblo Mall, Stanford, CA 94305, USA*

²*Kavli Institute for Particle Astrophysics & Cosmology, P. O. Box 2450, Stanford University, Stanford, CA 94305, USA*

³*Kavli Institute for Astrophysics and Space Research, Department of Physics, MIT, Cambridge, MA 02139, USA*

⁴*The NSF AI Institute for Artificial Intelligence and Fundamental Interactions, Massachusetts Institute of Technology, Cambridge, MA 02139, USA*

⁵*Center for Astrophysics | Harvard & Smithsonian, 60 Garden Street, Cambridge, MA 02138, USA*

⁶*Department of Mechanical Engineering, Columbia University, NYC, NY 10027, USA*

Accepted ***, Received ***; in original form ***

ABSTRACT

We investigate how feedback and environment shapes the X-ray scaling relations of early-type galaxies (ETGs), especially at the low-mass end. We select central-ETGs from the IllustrisTNG-100 box that have stellar masses $\log_{10}(M_*/M_\odot) \in [10.7, 11.9]$. We derive mock X-ray luminosity ($L_{X,500}$) and spectroscopic-like temperature ($T_{sl,500}$) of hot gas within R_{500} of the ETG haloes using the MOCK-X pipeline. The scaling between $L_{X,500}$ and the total mass within 5 effective radii (M_{5R_e}) agrees well with observed ETGs from Chandra. IllustrisTNG reproduces the observed increase in scatter of $L_{X,500}$ towards lower masses, and we find that ETGs with $\log_{10}(M_{5R_e}/M_\odot) \leq 11.5$ with above-average $L_{X,500}$ experienced systematically lower cumulative kinetic AGN feedback energy historically (vice versa for below-average ETGs). This leads to larger gas mass fractions and younger stellar populations with stronger stellar feedback heating, concertedly resulting in the above-average $L_{X,500}$. The $L_{X,500}$ – $T_{sl,500}$ relation shows a similar slope to the observed ETGs but the simulation systematically underestimates the gas temperature. Three outliers that lie far below the L_X – T_{sl} relation all interacted with larger galaxy clusters recently and demonstrate clear features of environmental heating. We propose that the distinct location of these backsplash ETGs in the L_X – T_{sl} plane could provide a new way of identifying backsplash galaxies in future X-ray surveys.

Key words: Galaxies: elliptical and lenticular, cD – X-rays: galaxies: clusters – galaxies: clusters: intracluster medium – methods: numerical

1 INTRODUCTION

Scaling relations are fundamental modalities between different physical properties of a certain class of astrophysical objects. Understanding these scaling relations is crucial to understanding the core physics that govern the formation and evolution of these objects. Over the past few decades, scaling relations for galaxy clusters have been studied extensively with a lush set of multiple frequency band observations. These relations mainly relate cluster mass estimates from weak lensing (von der Linden et al. 2014; Mantz et al. 2015; Hoekstra et al. 2015) to their electromagnetic signal in the X-ray (Vikhlinin et al. 2009; Mantz et al. 2010b, 2016), millimeter (Bleem et al. 2015; Planck Collaboration et al. 2016b; Hilton et al. 2018) and optical (Eisenstein et al. 2011; Rykoff et al. 2014, 2016; Abbott et al. 2018) wavelengths. Studying these scaling relations have significantly improved our understanding of galaxy formation at the high-mass end (Bryan & Norman 1998; Kravtsov & Borgani 2012)

as well as enabling more precise cluster cosmology with better halo mass estimation (Mantz et al. 2010a; Allen et al. 2011).

Extending these scaling relations from galaxy clusters to the massive galaxies is both challenging and important for understanding the formation of massive galaxies. Thanks to recent dedicated efforts targeting early-type galaxies (ETGs, e.g. Kormendy et al. 2009), observers are now starting to study ETG scaling relations at a similarly detailed level as galaxy clusters. It is found that ETG mass and their relatively hot interstellar medium (ISM) and circumgalactic medium (CGM) also follow scaling relations, although in most cases with different slope and scatter from those of groups and clusters. These include the X-ray luminosity–mass relation (O’Sullivan et al. 2001; David et al. 2006; Boroson et al. 2011; Kim & Fabbiano 2013; Sarzi et al. 2013; Kim & Fabbiano 2015; Goulding et al. 2016; Forbes et al. 2017; Babyk et al. 2018; Kim et al. 2019b), X-ray luminosity–temperature relation (David et al. 2006; Boroson et al. 2011; Kim & Fabbiano 2015; Goulding et al. 2016; Babyk et al. 2018; Kim et al. 2019b), and temperature–mass relation (O’Sullivan et al. 2003; Goulding et al. 2016; Babyk et al. 2018). The latest data products from Chandra also provide 2D spectral maps of the X-ray gas in ETGs (Kim et al. 2019a), enabling analyses of the spatial distribu-

* E-mail: ycwang19@stanford.edu

tion and dynamical properties of hot gas in ETGs. Diverse shapes of gas temperature profiles have been found from these X-ray spectral maps which indicate distinct sources of internal (feedback) and external (environment) heating being present for the X-ray gas in ETGs (Kim et al. 2020).

Interestingly, many of these recent studies (Kim & Fabbiano 2013, 2015; Goulding et al. 2016; Kim et al. 2019b) also found that the scatter in these ETG X-ray scaling relations tends to increase towards lower masses ($\log_{10}(M_{5R_c}/M_\odot) \leq 11.5$). This indicates potential secondary processes driving the differences in the luminosity and temperature of the ISM and CGM at a fixed mass scale. While White & Sarazin (1991) found that galaxies at a fixed *B*-band luminosity often have lower X-ray luminosity in denser environments, more recent literature (e.g. Goulding et al. 2016) finds a negligible correlation between the scatter in gas temperature and environment. Since supernova feedback (along with other types of stellar feedback, e.g., Springel & Hernquist 2003; Springel et al. 2005; Ceverino & Klypin 2009) and active galactic nuclei feedback (AGN, e.g., Di Matteo et al. 2005; Croton et al. 2006; Fabian 2012) can act as heat sources and drive outflows of the ISM and CGM, their interplay could lead to the observed scatter in X-ray luminosity or temperature (Babyk et al. 2018).

However, the debate is still open in both observational and theoretical fronts on whether stellar or AGN feedback is the dominant source of the low-mass-end scatter for ETG X-ray scaling relations. David et al. (2006), using a heating rate argument, suggested that Supernova Ia (SNIa for short) feedback dominates over AGN feedback in gas heating and driving outflows in low mass ETGs from Chandra. Similarly, Pellegrini (2011) argued for SNIa as the dominant source of internal gas heating using semi-analytic modeling in massive ETGs. Nevertheless, Choi et al. (2015) found in cosmological hydrodynamic simulations that a combination of kinetic and thermal AGN feedback can significantly reduce ETG X-ray luminosity at fixed mass. Forbes et al. (2017) further compared ETGs from the SLUGGS survey to Choi et al. (2015) and concluded that AGN is the main secondary factor that affects L_X in low-mass ETGs. Ciotti et al. (2017), using 2D magneto-hydrodynamic zoom-in simulations of individual ETGs, suggested that SNIa and AGN affect distinct aspects of the ETG gas: while gas heating is dominated by SNIa, AGN feedback significantly reduces L_X . Kim et al. (2019b) further supports the stellar feedback-driven heating scenario where Chandra-observed ETGs with higher stellar masses tend to have higher L_X at fixed dark matter halo masses. Moreover, Kim et al. (2020) found that hot gas cores in Chandra ETGs are mostly related to recent star formation and hence stellar feedback is dominant instead of AGN feedback or gravitational heating. In addition to stellar and AGN feedback, other physical differences such as the inner density profile or the dynamical state (Pellegrini 1999; Sarzi et al. 2013; Kim & Fabbiano 2015; Kauffmann et al. 2019) of the ETG can also lead to systematic differences in X-ray luminosities at the low-mass end, pointing to secondary heating effects from galactic rotation and the shape of the gravitational potential which could also add to the low-mass-end scatter.

Advancements in cosmological simulations over the past two decades have revolutionized our understanding of galaxy evolution (see e.g. Vogelsberger et al. 2020a for a review). To further elucidate the origin of these ETG X-ray scaling relations, we use a legacy ETGs sample (Wang et al. 2020) from the cosmological hydrodynamic simulation IllustrisTNG, which is an updated version of the Illustris Project (Vogelsberger et al. 2014a,b; Genel et al. 2014; Sijacki et al. 2015; Nelson et al. 2015), and that has well-studied density profile, stellar properties, and dark matter fractions (Lovell et al. 2018; Wang

et al. 2019, 2020, 2022). Our work further extends the previous X-ray scaling relation studies using IllustrisTNG (e.g., X-ray scaling relations for star-forming and quenched galaxies: Truong et al. 2020; the relation of black hole growth to CGM properties: Oppenheimer et al. 2020; Truong et al. 2021; X-ray scaling relations in galaxy groups and clusters: Pop et al. 2022) by especially focusing on the formation mechanisms leading to the scatter at the low-mass-end. Our work is also complementary to these previous X-ray scaling relation studies as we examine outliers showing clear signs of environmental (shock) heating which has important implications for future X-ray surveys.

This paper is organized as follows. In Section 2 we describe the general information of the simulation, how the mock ETG sample is selected, and how the mock X-ray properties of the hot gas in these ETG parent haloes are extracted. In Section 3 we present the key results of our analysis including the X-ray scaling relations as well as the physical processes that contribute to shaping these relations. In Section 4 we present the formation history for outliers of the X-ray luminosity-temperature relation and how they can be used to identify backplash objects. Finally in Section 5, we provide a brief summary of this work.

2 METHODOLOGY

2.1 Simulation overview

The Next Generation Illustris simulations (Marinacci et al. 2018; Naiman et al. 2018; Nelson et al. 2018; Pillepich et al. 2018b; Springel et al. 2018; Nelson et al. 2019b; Pillepich et al. 2019), a.k.a. IllustrisTNG, is a suite of magneto-hydrodynamic simulations run with the publicly-available moving-mesh code AREPO (Springel 2010; Weinberger et al. 2020). It steps up from the original Illustris Simulations (Vogelsberger et al. 2013; Torrey et al. 2014; Vogelsberger et al. 2014a,b; Genel et al. 2014; Sijacki et al. 2015; Nelson et al. 2015) and improves upon the sub-grid physics of the stellar and AGN feedback models (Weinberger et al. 2017; Pillepich et al. 2018a). These improvements lead to more realistic predictions in terms of observed galaxy properties and demonstrates the capacity of IllustrisTNG to shed light on the underlying physical processes shaping these properties. Some of the comparison works with observations include the galaxy mass–metallicity relation (Torrey et al. 2018, 2019), the galaxy-color bimodality in the Sloan Digital Sky Survey (Nelson et al. 2018), the intra-cluster metal distribution (Vogelsberger et al. 2018), early-type galaxy total density profiles (Wang et al. 2020), gas-phase metallicity gradients in star-forming galaxies (Hemler et al. 2021), stellar orbital fraction and outer kinematic structure (Xu et al. 2019; Wang et al. 2022), optical morphologies of galaxies (Rodriguez-Gomez et al. 2019), the size evolution of galaxies (Genel et al. 2018), star formation activities and quenched fractions (Donnari et al. 2019), spatially-resolved star formation in galaxies (Nelson et al. 2021), the fraction of cool-core clusters (Barnes et al. 2018), as well as AGN galaxy occupation and X-ray luminosities (Weinberger et al. 2018; Habouzit et al. 2019; Terrazas et al. 2020), and predictions of high redshift galaxy luminosity functions for JWST (Vogelsberger et al. 2020b). Although certain aspects of these predictions are still discrepant with observations, the broad agreement in many properties related to gas cycle, star formation, and feedback lends us generous predicative power to gain insights on the key factors that shape the X-ray scaling relations in ETGs. The simulation adopts Planck-2016 flat- Λ CDM cosmology (Planck Collaboration et al. 2016a) with parameters of $h = 0.6774$, $\sigma_8 = 0.8159$, $\Omega_m = 0.3089$, $\Omega_b = 0.0486$, and $\Omega_\Lambda = 0.6911$.

2.2 Sample selection

We select massive (stellar mass $\log_{10}(M_*/M_\odot) \in [10.7, 11.9]$) early-type central galaxies from the TNG100-1 box. This is the highest resolution simulation box that has a side length of 75 Mpc/h, with 2×1820^3 resolution elements for baryons and dark matter particles. The mass resolution of baryons and dark matter are $m_{\text{baryon}} = 1.4 \times 10^6 M_\odot$ and $m_{\text{DM}} = 8.9 \times 10^6 M_\odot$, respectively. This places the TNG100-1 box at a sweet spot for our purpose among the 35 Mpc/h and 205 Mpc/h side length boxes, which provides an abundant sample of well-resolved massive galaxies. The softening scale of gas cells are fully adaptive (minimum 0.19 kpc) while a fixed softening length of $\epsilon = 0.74$ kpc is applied to dark matter and stellar particles. All simulation data used for this analysis is publicly available (Nelson et al. 2019a).¹

We adopt the early-type galaxy classification method documented in Xu et al. (2017) to select our simulated ETGs. The final ETG galaxy sample with 559 galaxies is identical to the one used in Wang et al. (2020) and we briefly outline the selection procedure. To begin with, the stellar component of the largest gravitationally bound object (found by SUBFIND Springel et al. 2001; Dolag et al. 2009) in a Friends-of-Friends (FoF) group is defined as the ‘central’ galaxy. An age and metallicity-dependent magnitude is assigned to stellar particles based on their intrinsic luminosity using the stellar population synthesis (SPS) model GALAXEV (Bruzual & Charlot 2003). We also apply a semi-analytic dust attenuation model as in Xu et al. (2017) to account for dust absorption, emission, and scattering.

The main classification criterion for a central galaxy to be early-type is based on their SDSS *r*-band rest-frame luminosity profiles. We perform both single and double-component luminosity profile template fitting to enable more robust classification. The single-component fit consists of fitting either exponential (Sérsic $n = 1$) or de Vaucouleurs (Sérsic $n = 4$) profile templates. The double-component fit combines a de Vaucouleurs and an exponential profile that has their relative ratio as a free parameter, which are better for galaxies that demonstrate prominent bulge-disk combinations. In the final sample, we only define galaxies as ETGs when they are not only better fitted by a single de Vaucouleurs profile but also have $> 50\%$ bulge ratio from the two-component fit in all three (box x, y, z axes) projections. This leads to a sample of 559 central ETGs in the mass range of $\log_{10}(M_*/M_\odot) \in [10.7, 11.9]$ (corresponding to $[3.6 \times 10^4, 5.8 \times 10^5]$ stellar particles) at $z = 0$. The M_{500} mass range for the host haloes of our selected ETGs is in the range of $\log_{10}(M_{500}/M_\odot) \in [11.79, 13.67]$.

2.3 The mock X-ray luminosity and gas temperature

We create mock X-ray luminosity (L_X) maps of the hot circumgalactic medium (CGM) in the parent halo of our selected central ETGs using MOCK-X² (Barnes et al. 2021). In each mock pixel, the code starts by generating an X-ray spectral template look-up table for the 11 elements tracked by the simulation in the temperature range $10^6 < (T/\text{K}) < 10^9$ (temperature resolution $\delta \log_{10}(T/\text{K}) = 0.02$) using APEC (Astrophysical Plasma Emission Code, Smith et al. 2001) and PYATOMDB using atomic data values from ATOMDB v3.0.9 (Foster et al. 2012). A synthetic X-ray spectrum for each gas cell is then sampled from this numerical table assuming a *Chandra* ACIS-I configuration with an energy range of $0.5 < (E/\text{keV}) < 10$ and energy

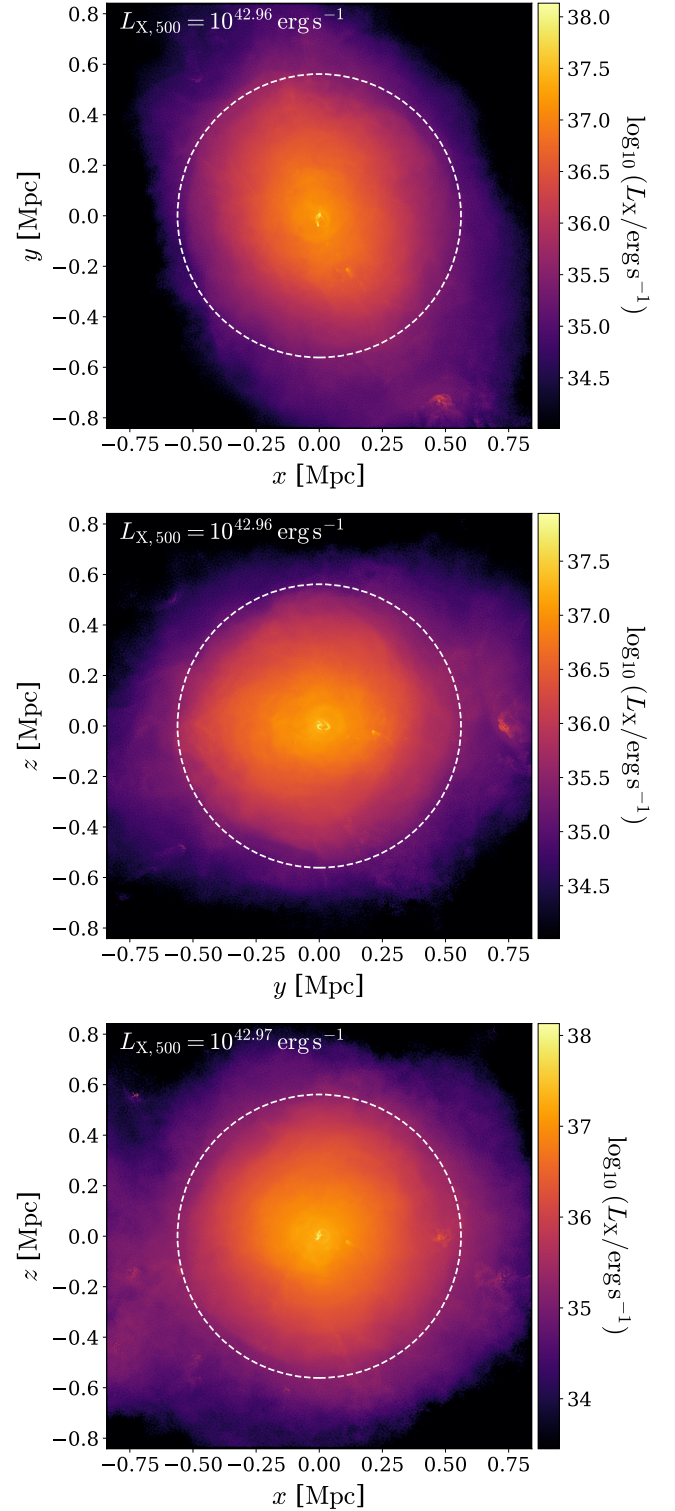


Figure 1. The projected L_X distribution of the hot circumgalactic gas in the host halo of our most massive ETG as a demonstration of the MOCK-X pipeline output. The projections in the z, x, y directions along the simulation box axes are shown from top to bottom. In each panel, the color map indicates the total X-ray luminosity projected in each pixel, while the dashed circle marks the size of the halo R_{500} . We also label the total X-ray luminosity projected within a 2D aperture with the size of R_{500} at the top left corner of each subplot.

¹ <https://www.tng-project.org/>

² https://bitbucket.org/djbarnes_88/mock-x_public/src/master/

resolution of 150 eV. Cold ($T < 10^6$ K), star-forming, or actively cooling gas cells are removed in the calculation. We also apply a correction for the galactic absorption assuming a constant neutral hydrogen column density of $n_{\text{H}} = 2 \times 10^{20} \text{ cm}^{-2}$. Finally, the projected X-ray luminosity maps are created along the x, y, z axes of the simulation box within a circular aperture of $3R_{500}$ (3 times the radius within which the mean matter density is 500 times the cosmic critical density).

In Fig. 1, we show the projected X-ray luminosity map for the hot gas in the host halo of the most massive galaxy in our ETG sample. From top to bottom, the x, y, z projections are shown respectively. The dashed circle indicates the size of the halo R_{500} (radius within which the average density of the halo is 500 times that of the critical density of the universe). The resolution (0.492 arcsec) and observational band (soft and medium X-ray, 0.5–2.0 keV) of the maps have been set identical to that of Chandra, which we apply to the whole sample of our selected ETGs. In our following analysis, we sum the L_{X} values for all pixels that fall within R_{500} in the x projection as our $L_{\text{X},500}$ measurement.

As for the X-ray temperature of our massive ETG sample, the minimum temperature of gas cells can fall below 10^6 K (~ 0.1 keV), which makes the MOCK-X spectroscopic fitting via APEC table interpolation unreliable (since it was originally designed for cluster scale temperatures). Instead, we implement an approximate X-ray temperature reconstruction for the hot gas in our massive ETGs following the spectroscopic-like temperature definition in Mazzotta et al. (2004). Specifically, we construct spectroscopic-like temperature maps with the same projected spatial grid as the L_{X} maps mentioned above, but with each pixel weighted by the combination of gas density and temperature:

$$T_{\text{sl}} = \frac{\int (n_{\text{H}}^2 T^{-3/4}) T dV}{\int (n_{\text{H}}^2 T^{-3/4}) dV} = \frac{\sum_i n_{\text{H},i}^2 T_i^{1/4} V_i}{\sum_i n_{\text{H},i}^2 T_i^{-3/4} V_i}, \quad (1)$$

where $n_{\text{H},i}$, T_i and V_i are the hydrogen number density, temperature, and Voronoi cell volume of the i -th gas cell. The summation is conducted over all gas cells that have an overlap (after accounting for their smoothing length) with the pixel in question. To avoid significant bias introduced by cold-dense gas cells to the spectroscopic-like temperature, we remove all gas cells with temperature $T_i < 0.05$ keV ($\sim 5.8 \times 10^5$ K), number density $n_{\text{H},i} > 0.1$, or star formation rate $\text{SFR} > 0$ in the calculation of all the spectroscopic-like temperature map calculations. This cut removes gas cells that are interacting with the Equation of State and avoids the $T < 0.05$ keV temperature range where spectroscopic-like temperature becomes more inaccurate. We then average over all gas cells with 3D distances $< R_{500}$ to the galaxy center and derive the average halo $T_{\text{sl},500}$ for each ETG.

3 RESULTS

3.1 X-ray scaling relations of the simulated ETGs

We present the scaling relation between the X-ray luminosity ($L_{\text{X},500}$) and the mass or gas temperature ($T_{\text{sl},500}$) of our mock ETGs in Fig. 2. We perform linear fit with outlier clipping using the `LTS_LINEFIT` program³ for both scaling relations. The blue dots in the figure mark the mock ETGs that are kept after the clipping, while the outliers (outside of the 2.6σ confidence interval) are denoted

with green dots. We assume a fiducial 0.1 dex uncertainty in the mass and spectroscopic-like temperature measurements, and 0.2 dex uncertainty in the X-ray luminosity.

The left panel shows the scaling relation of $L_{\text{X},500}$ with the total mass (dark matter, gas, and stars combined) within five times the 2D effective radii (R_e) of the central ETGs. There are no significant outliers for our sample and indicates a rather tight linear relation. The dotted-dashed grey line along with the grey band showcases the mean and 1σ scaling relation fit to Chandra-observed ETGs (Kim et al. 2019b). The observers derived ETG dynamical masses using globular cluster (GC) kinematics (Alabi et al. 2017) or GC photometric scaling relations (Harris et al. 2013, 2017) out to $5R_e$ and we adopt the same radii for the mass definition of the simulated ETGs. The IllustrisTNG ETGs show great agreement with the observations in terms of both the slope and the scatter of the scaling relation, which is also a significant improvement over past hydrodynamic simulations (e.g. Choi et al. 2015) thanks to the updated IllustrisTNG AGN and stellar feedback models. An interesting feature is that the scatter for the simulated ETGs seems to increase towards lower masses, which we investigate further in the following sections (3.2, 3.3).

The right panel of Fig. 2 shows the scaling relation between $T_{\text{sl},500}$ and $L_{\text{X},500}$ of the simulated ETGs, which also demonstrates a tight linear relation for most of the points. The two observed ETG samples we compare to are both from integral-field-unit surveys with spatially-resolved stellar kinematics while also being in the Chandra archival footprint. Our best-fit log-linear slope of 5.74 is closer to the 61 ATLAS^{3D} (Cappellari et al. 2011) E and S0 galaxy sample (slope of 5.4, Kim & Fabbiano 2015) as compared to that of 33 early-type galaxies (slope of 4.7, Goulding et al. 2016) from the MASSIVE Survey (Ma et al. 2014). The agreement in the $L_{\text{X}}-T_{\text{sl}}$ slope with observations for a statistical sample of simulated ETGs from a 3D cosmological simulation is also a big step up from previous hydro-simulation results such as Ciotti et al. (2017) who used 2D zoom-in approaches.

Although the slope of the simulated ETGs is close to the observationally-derived values, the mean temperature at fixed $L_{\text{X},500}$ for IllustrisTNG is ~ 0.5 dex lower than the observed ETGs. Since the $L_{\text{X},500}-M_{\text{tot}}(<5R_e)$ relation closely resembles the observed scaling relations, this systematic offset is mainly due to a factor ~ 3 colder CGM in IllustrisTNG ETGs (the dotted-dashed blue line in the right panel of Fig. 2 matches well with observations), that are most likely due to limitations in the current AGN feedback model and will require future improvements to alleviate the discrepancy. Pop et al. (2022) found a similar issue with IllustrisTNG (in TNG300) predicting cooler X-ray temperatures of gas than in observations (see their section 4.3 for a discussion on potential model limitations). They found that the spectroscopic temperature derived from MOCK-X in a more massive sample ($M_{500} > 10^{13} M_{\odot}$, $T_{\text{X,spec}} > 0.5$ keV where spectroscopic template fitting is reliable) is systematically underestimated by a factor ~ 2 , which is consistent with the ~ 0.3 dex underestimation seen in our sample at the high- T_{sl} end. The spectroscopic-like temperature definition further enhances the underestimation due to the $T^{-3/4}$ weighting, and that underestimation is actually a bit stronger in IllustrisTNG compared to other cosmological hydrodynamic simulations (see Figure A5 in Lee et al. 2022).

Despite the cooler-than-observed temperatures for most of our simulated ETGs, there are three significant outliers in $T_{\text{sl},500}$ at the low $L_{\text{X},500}$ end (Fig. 2 right panel). Similar high temperature outliers were also seen in observed scaling relations (see e.g. Figure 2 right panel in Kim & Fabbiano 2015). Although observational uncertainties are large at the faint end, observed ETGs tend to up-scatter more in temperature at fixed low L_{X} ($\sim 10^{38} - 10^{39} \text{ ergs s}^{-1}$), which is in

³ <https://www-astro.physics.ox.ac.uk/~mxs/software/#lts>

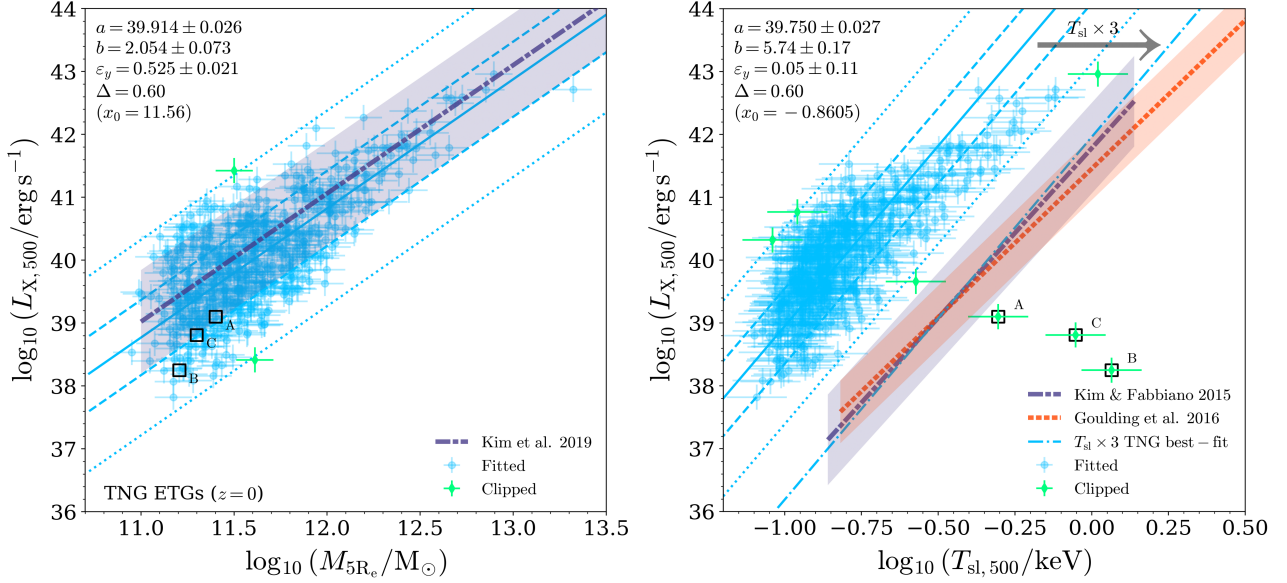


Figure 2. X-ray scaling relations. *Left panel:* The total X-ray luminosity projected within R_{500} ($L_{X,500}$) versus the total mass within $5R_e$ (M_{5R_e}) of the central ETG. Colored dots with error bars are IllustrisTNG ETGs with fiducial 0.1 and 0.2 dex uncertainties applied to mass and luminosity mimicking observational uncertainties. The solid, dashed, and dotted blue lines are the best fit scaling relation, 1σ , and 2.6σ confidence intervals for the simulated ETGs. The blue dots are ETGs within the 2.6σ (99%) confidence interval, while green dots are outliers. The purple dotted-dashed line and band shows the best-fit scaling relation and the 1σ confidence interval from Chandra (Kim et al. 2019b). The best fit slope (b), intercept (a), and scatter (Δ) for the IllustrisTNG scaling relation are also labelled in the plot. The three black squares correspond to the three extreme outliers in the right panel. *Right panel:* Similar to the left panel, but for the ‘spectroscopic-like’ temperature $T_{\text{sl},500}$ versus $L_{X,500}$ scaling relation. Fiducial uncertainties of 0.1 dex are applied to the $T_{\text{sl},500}$ values. The latest scaling relations for observed ETGs that we compare to are from Kim & Fabbiano (2015); Goulding et al. (2016). The three outliers we study in Section 4 that have significantly higher $T_{\text{sl},500}$ than their siblings with similar $L_{X,500}$ are marked by the black squares. We also plot dotted-dashed blue the best-fit L_X – T_{sl} relation for IllustrisTNG ETGs with the temperature multiplied by 3 for a clearer comparison of the scaling relation slope to observations.

the same $L_{X,500}$ range as our outliers. Since they are all below the best-fit $L_{X,500}$ – M_{5R_e} relation, we conjecture they are all influenced by galaxy interactions that caused gas stripping. We thoroughly investigate the merger histories of these three outliers in Section 4 and we identify these outliers as backsplash galaxies that have recently been through significant tidal interactions and environmental heating.

3.2 The scatter in $L_{X,500}$ and the dark matter fraction

In this section, we discuss the correlation between the offset from the best-fit $L_{X,500}$ – M_{5R_e} scaling relation and the dark matter fraction within $5R_e$ of the IllustrisTNG ETGs. The offset $\Delta L_{X,500}$ is calculated as the difference between the IllustrisTNG ETG data points and their linear fit (black line) in Fig. 2. This is a natural way of quantifying the scatter off of the mean scaling relation following Kim et al. (2019b), while it also allows for characterizing secondary effects that affect L_X other than the primary factor, total mass. Kim et al. (2019b) found that for Chandra ETGs with $\log_{10}(M_{5R_e}/M_{\odot}) < 11.5$, those that up-scatter in $L_{X,500}$ at fixed total mass tend to have lower dark matter fraction (and vice versa for down-scattering $L_{X,500}$ ETGs, see their Figure 8 for details). This effect is stronger for cuspy Chandra ETGs (compared to cored ones) which are often fast rotators possessing younger stellar populations. They suggested that this difference for cuspy versus cored ETGs could be linked to differences in the strengths of stellar feedback in the two types of systems.

In the left panel of Fig. 3, we plot the $L_{X,500}$ – M_{5R_e} scaling relation colored by $1 - f_{\text{star}} (\leq 5R_e)$ for IllustrisTNG ETGs. The blue dashed box indicates the galaxies with $\log_{10}(M_{5R_e}/M_{\odot}) \leq 11.5$, and at face

value there is no significant vertical trend with $1 - f_{\text{star}}$ for galaxies above or below the linear fit. This is qualitatively different than in the Kim et al. (2019b) sample (their Figure 8), however we do notice that their observed ETGs above the linear fit typically have $f_{\text{DM}} < 0.5$, while the simulated ETGs have $f_{\text{DM}} \gtrsim 0.6$. In Appendix A we show that selecting ‘relaxed’ and ‘unrelaxed’ host haloes for our selected ETGs does not impact the range of their dark matter fractions, such that these high dark matter fractions are not artifacts of mis-centered ETGs residing in unrelaxed haloes.

In the right panel of Fig. 3, we plot the offset from the linear fit of the X-ray luminosity/total mass scaling relation, $\Delta L_{X,500}$, against the combined gas and dark matter mass fraction, $1 - f_{\text{star}} (\leq 5R_e)$, for *all* simulated ETGs. This definition follows Kim et al. (2019b) where they assumed the gas mass fraction to be negligible compared to dark matter and defined $f_{\text{DM}} = 1 - f_{\text{star}}$ as a proxy for dark matter fraction. Our IllustrisTNG sample has gas mass fractions typically less than 1% (median 0.8%) which agrees with their assumption (also see top left panel in Fig. 4). We also overplot the 61 observed ETGs from Kim et al. (2019b) Figure 11 for comparison. The linear fits to the simulation and observation samples yield similar slopes and both show robust (very small Pearson p values as labelled in the plots) negative correlations between $1 - f_{\text{star}}$ and $\Delta L_{X,500}$. At $1 - f_{\text{star}} \gtrsim 0.6$, the simulation also shows a similar level of scatter of $\Delta L_{X,500}$ (0.59 dex) as compared to observations (0.74 dex). Therefore, although IllustrisTNG reproduces the negative correlation between $\Delta L_{X,500}$ and the dark matter fraction, the compressed range of $1 - f_{\text{star}}$ leads to the lack of apparent correlation between $L_{X,500}$ and $1 - f_{\text{star}}$ in the top left panel of Fig. 3, especially for ETGs with $\log_{10}(M_{5R_e}/M_{\odot}) <$

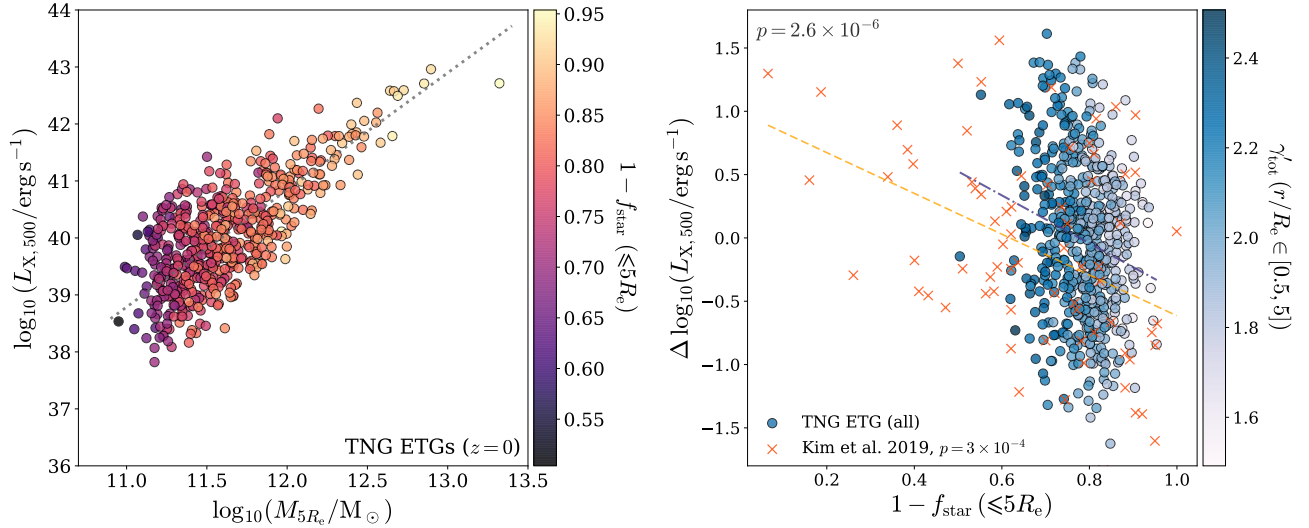


Figure 3. *Left panel:* The $L_{X,500}$ – M_{5R_e} scaling relation colored by the combined dark matter and gas mass fraction within $5R_e$, $1 - f_{\text{star}} (\leq 5R_e)$. The grey dashed line denotes the linear fit to the $L_{X,500}$ – M_{5R_e} scaling relation (same as the solid blue line in the left panel of Fig. 2). *Right panel:* The offset in the $L_{X,500}$ from the best-fit $L_{X,500}$ – M_{5R_e} scaling relation, $\Delta L_{X,500}$, versus $1 - f_{\text{star}} (\leq 5R_e)$. The orange markers are observed ETGs from Kim et al. (2019b), while the orange dashed line is the linear fit to them. The color map for the scattered points indicates the power-law slope of the simulated ETG total density profiles measured in 3D spherical shells from $0.5R_e$ to $5R_e$. The blue dotted-dashed line is the linear fit to the IllustrisTNG ETGs with a Pearson $p = 2.6 \times 10^{-6}$, indicating a clear correlation between $L_{X,500}$ and $1 - f_{\text{star}}$ as in observations. However, the simulated ETGs have systematically large dark matter fractions than Chandra ETGs and their ΔL_X show no clear correlation with their density profile slope γ'_{tot} .

11.5, where simulated ETGs both above and below the mean X-ray luminosity-mass relation can have similar $1 - f_{\text{star}}$.

Observationally-derived dark matter fractions are not free from systematics, and the range of dark matter fraction values can be dependent on the specific approach used for measuring the total mass of the ETGs. Lovell et al. (2018) compared dark matter fractions within $5R_e$ of IllustrisTNG galaxies to observations (top left panel of their Figure 12). IllustrisTNG showed better agreement with Wojtak & Mamon (2013) who used satellite galaxy kinematics compared to Alabi et al. (2017) who used GC kinematics. Since most of the ETG masses in Kim et al. (2019b) come from GC kinematics in Alabi et al. (2017), the tendency for ETGs in Kim et al. (2019b) to have lower dark matter fractions than IllustrisTNG ETGs is consistent with expectations. Thus, if one adopted satellite kinematics-based dark matter fractions (mostly larger than 50%) from Wojtak & Mamon (2013) for the observed ETGs, the correlation between $\Delta L_{X,500}$ and $1 - f_{\text{star}}$ would likely weaken or even disappear.

As Kim et al. (2019b) discovered that ΔL_X varies differently with $1 - f_{\text{star}}$ for cuspy versus cored ETGs, we investigate the systematic trends of $\Delta L_{X,500}$ with the total mass density profile for our simulated ETGs. Systematic covariance in dark matter fraction and total density profiles of ETGs is well-studied through observed stellar kinematics modeling (Thomas et al. 2007; Tortora et al. 2014; Poci et al. 2017; Bellstedt et al. 2018; Derkenne et al. 2021), strong gravitational lensing (Auger et al. 2010; Ruff et al. 2011; Barnabè et al. 2011; Sonnenfeld et al. 2013; Shajib et al. 2021; Etherington et al. 2022), and in hydrodynamic simulations (Remus et al. 2017; Xu et al. 2017; Wang et al. 2020). The color map for the right panel of Fig. 4 shows the power-law slope (γ'_{tot}) of the total density profile of all the IllustrisTNG ETGs measured in 100 logarithmic bins from $0.5R_e$ to $5R_e$. The color gradient in γ'_{tot} is mainly visible along the $1 - f_{\text{star}}$ direction, while ETGs having different $\Delta L_{X,500}$ at fixed $1 - f_{\text{star}}$ do not seem to have drastically different density profiles. This indicates that the total density profile, at least down to $0.5R_e$

(limited by the simulation softening scale), does not play a dominant role in driving the scatter in $L_{X,500}$ of our IllustrisTNG ETG sample. Future higher resolution cosmological simulations that can resolve the inner density profiles for a large number of ETGs down to $0.1R_e$ would be desirable for further disentangling the X-ray gas properties of cuspy versus cored ETGs.

3.3 The impact of AGN feedback

In this section, we discuss how variations in the cumulative kinetic (wind) mode AGN feedback energy for our IllustrisTNG ETGs drives the scatter in $L_{X,500}$ at the low-mass end, meanwhile also leading to covariances in gas fractions, stellar ages, and recent AGN activities for these low-mass ETGs.

Supermassive blackholes (SMBH) at the centers of haloes can regulate gas properties including temperature and cooling timescales. Since the CGM (including the ISM within the central galaxy) is directly impacted by active galactic nucleus (AGN) feedback, we expect the effects of AGN feedback to also manifest in the scatter of $L_{X,500}$ for ETGs. The IllustrisTNG AGN feedback model (Weinberger et al. 2017, 2018) features two channels: the radiative (pure thermal) mode that resembles high-accretion-rate thermal feedback common to high redshift quasars, and the low-accretion-rate kinetic mode that approximates centrally driven winds in quiescent AGN (no thermal energy injection). The former deposits thermal energy isotropically to the surrounding ISM of the central SMBH, while the latter injects kinetic kicks to the surrounding gas in random directions. For massive galaxies with $M_* \gtrsim 10^{11} M_{\odot}$, the kinetic mode AGN feedback energy becomes the dominant feedback channel over the radiative mode at $z = 0$ (Zinger et al. 2020). Choi et al. (2015) also found that thermal AGN feedback alone cannot bring down L_X to observed values, and kinetic AGN feedback must be incorporated in order to further decrease L_X matching observed ETG X-ray scaling relations. Indeed, as we show in Appendix B, this is also the

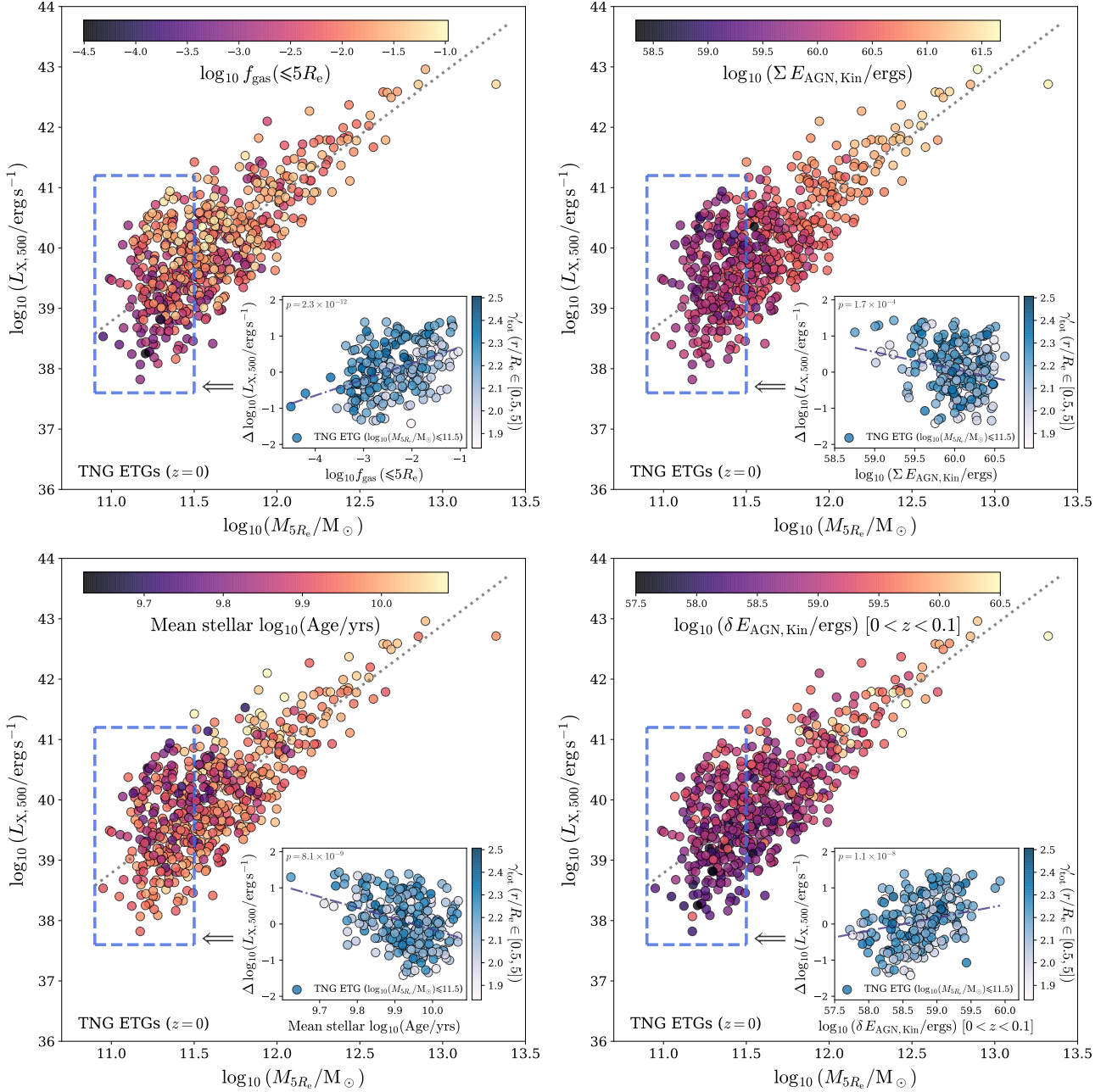


Figure 4. The $L_{X,500}$ – M_{5R_e} scaling relation colored by the total gas mass fraction (f_{gas} , *top left*), the cumulative kinetic mode AGN feedback energy from their central SMBHs ($\Sigma E_{\text{AGN, Kin}}$, *top right*), the mean stellar age of stars (*bottom left*), and the kinetic mode AGN feedback energy in the past 1.3 Gyr ($\delta E_{\text{AGN, Kin}} [0 < z < 0.1]$, *bottom right*). In each panel, the grey dashed line denotes the linear fit to the $L_{X,500}$ – M_{5R_e} scaling relation in the left panel of Fig. 2. The blue dashed boxes in each panel marks out the low-mass region ($\log_{10}(M_{5R_e}/M_{\odot}) \leq 11.5$) we focus on exploring the scatter in X-ray luminosity, and there are clear correlations between $L_{X,500}$ and the colored physical quantities in every box. In the *inset panels* for each subplot, we show the offset in the $L_{X,500}$ from the best-fit $L_{X,500}$ – M_{5R_e} scaling relation, $\Delta L_{X,500}$, versus the *color bar* physical quantities for ETGs in the blue boxes. The blue dotted-dashed line in each inset plot is the linear fit to the low-mass ETGs with their Pearson p values labelled at the top left corner of each inset. The color maps for the inset panels indicate the power-law slope of the total density profiles for these low-mass ETGs measured from $0.5R_e$ to $5R_e$. We truncate the x axis lower limit at 57.5 for the bottom right inset panel to focus on the main distribution of data points in our sample, but this truncation does hide 4 ETGs with $\log_{10}(\delta E_{\text{AGN, Kin}}/\text{ergs}) < 57.5$. The four *inset panels* further corroborate the significant correlations between $\Delta L_{X,500}$ and the four colored physical quantities in the main plots.

case for our IllustrisTNG simulated ETG sample, such that the radiative AGN feedback energies do not significantly impact the scatter in $L_{X,500}$, and most of the SMBHs for our sample are thermally quiescent at $z < 0.1$ (see middle and bottom panels of Fig. B1). Furthermore, through radiative heating, turbulence injection, kinetic

expulsion of gas through winds, AGN feedback also lowers the star formation efficiency of gas in the central galaxy and becomes the dominant factor for quenching in massive central galaxies (Donnari et al. 2021; Piotrowska et al. 2022).

In Fig. 4, we show how AGN feedback and its consequences on

gas properties and star formation influences $L_{X,500}$, especially the scatter at $\log_{10}(M_{5R_e}/M_\odot) \leq 11.5$. The color maps include the gas mass fraction within $5R_e$ (f_{gas} , top left), the mean stellar age (bottom left), cumulative feedback energy in the kinetic mode of the central SMBH ($\Sigma E_{\text{AGN,Kin}}$, top right), and the kinetic mode feedback energy of the central SMBH from $z = 0.1$ to $z = 0$ (~ 1.3 Gyrs, $\delta E_{\text{AGN,Kin}}$, bottom right). In the low-mass region with $\log_{10}(M_{5R_e}/M_\odot) \leq 11.5$ (blue dashed boxes, we refer to galaxies in this box as ‘low-mass ETGs’ in the following), $L_{X,500}$ shows clear correlations with all four colored physical quantities. In the inset plots of each panel, we further show for ETGs in the blue boxes their offset from the mean scaling relation $\Delta L_{X,500}$ versus their respective colored quantities in the main plots. The linear fits and the very small Pearson p -values of the fits in the insets demonstrate robust negative correlations between $L_{X,500}$ with mean stellar age and cumulative kinetic AGN feedback energy $\Sigma E_{\text{AGN,Kin}}$, as well as robust positive correlations with the gas fraction f_{gas} and recent AGN kinetic feedback $\delta E_{\text{AGN,Kin}}$ ($0 < z < 0.1$).

To self-consistently explain these four sets of systematic trends in the scatter of $L_{X,500}$ at the low-mass end, we argue that the cumulative kinetic feedback energy from their SMBH is the driving factor. In this scenario, lower mass ETGs that up-scatter in $L_{X,500}$ experienced less AGN kinetic feedback historically and retained a larger gas reservoir, leading to higher gas mass fraction. This is consistent findings in previous work using IllustrisTNG that the X-ray luminosity positively correlates with the CGM fraction in the mass range $\log_{10}(M_*/M_\odot) \in [10.8, 11.4]$ (Oppenheimer et al. 2020). The less-violent AGN (kinetic) feedback leads to younger stellar populations due to less efficient quenching. The consequence of having younger stars is stronger stellar feedback that can further heat up the ISM and CGM, leading to higher $L_{X,500}$. Moreover, the fact that these up-scatter ETGs in $L_{X,500}$ end up having larger f_{gas} also fuels more recent AGN accretion and hence higher recent feedback energies ($\delta E_{\text{AGN,Kin}}$).

Conversely, one could argue that stronger recent (instead of historic) AGN feedback or stellar feedback (star formation) is the dominant driver for creating the scatter in $L_{X,500}$ at the low-mass end. Since most of our ETGs have thermally quiescent AGN in the last 1.3 Gyrs (bottom panel of Fig. B1), stronger recent kinetic AGN feedback in up-scatter $L_{X,500}$ alone could not lead to hotter gas around these ETGs without effective radiation. If recent AGN kinetic feedback energy did have a significant impact on the ISM and CGM, the color gradients in the left two panels of Fig. 4 should revert, with up-scatter $L_{X,500}$ ETGs having lower f_{gas} and old stellar ages. Similarly, if stronger stellar feedback is the core driver of the scatter in $L_{X,500}$ at the low-mass end, it should also drive stronger outflows and lead to lower f_{gas} in up-scatter $L_{X,500}$ ETGs, which is opposite from the top left panel in Fig. 4. It will also be hard to explain why systematic variations in star formation or stellar feedback also simultaneously cause variations in the AGN feedback energies.

Furthermore, we check in Appendix B that $L_{X,500}$ and the SMBH mass M_{BH} do not have significant correlation for the low-mass ETGs with $\log_{10}(M_{5R_e}/M_\odot) < 11.5$. Thus, the variations in cumulative and recent AGN kinetic feedback energies in Fig. 4 are not driven by variations in SMBH mass, but rather the diverse accretion and merger histories of the SMBH leading to different feedback histories that shape the scatter in $L_{X,500}$. Our findings here are also consistent with the previous study of Truong et al. (2021), who showed that IllustrisTNG galaxies having $L_{X,500} \lesssim 10^{41} \text{ erg s}^{-1}$ have significantly larger scatter in M_{BH} at fixed L_X than galaxies with $L_{X,500} \gtrsim 10^{41} \text{ erg s}^{-1}$, leading to a weaker correlation between L_X and M_{BH} .

Although many observations suggest that the internal heating of X-ray gas in ETGs is driven by stellar feedback at low masses (David et al. 2006; Kim et al. 2019b, 2020), our findings above dive deeper and provide a more comprehensive picture about the fundamental physics behind the scatter in L_X . Weaker kinetic AGN feedback in the past could enhance star formation and gas fractions, leading to present-day younger stellar populations and as a consequence, drive stronger stellar feedback that heat up the gas. However, this is qualitatively different from stellar feedback being the intrinsic source of feedback that leads to higher L_X . Since observations are limited to static AGN properties, they may seem obvious when compared to observables (e.g. star formation rate, stellar ages, metallicity) that probe stellar feedback. We also point out that Boroson et al. (2011) observed a slightly positive correlation of L_X with stellar age at around K -band magnitude of $\sim 10^{11} L_\odot$, opposite from what we see in IllustrisTNG. Since they had only 7 galaxies, their result could suffer from small number statistics. But if future observations with better statistics still see older stellar populations in ETGs with larger L_X at fixed masses, it may suggest limitations in the current IllustrisTNG AGN model and advocate for more efficient radiative feedback at low redshift that can simultaneously quench star formation (older ages) and heat up the gas (higher L_X).

Finally, the color maps in the inset plots in Fig. 4 mark out the variations of the total density profile for the low-mass ETGs. There is no significant correlation between $\Delta L_{X,500}$ with the total density profile power-law slope. Reflecting on Wang et al. (2019), the evolution of the total density profile in massive ETGs are mainly dominated by gas-poor mergers at $z \lesssim 1$. AGN feedback only impacts the total density profile at $z \gtrsim 1$ when the ETGs were still quite gaseous, while the efficient kinetic mode feedback can impact the small fraction of diffuse gas all the way to $z = 0$, shaping $\Delta L_{X,500}$. These different physical origins of $\Delta L_{X,500}$ and γ'_{tot} at low redshift make their dis-correlation a natural outcome.

4 OUTLIERS OF THE L_X – T_{SL} RELATION: PROBING BACKSLASH

In this section we investigate the formation history of the three outlier ETGs of the $L_{X,500}$ – $T_{\text{sl},500}$ relation as indicated in the right panel of Fig. 2. We conjecture that these objects are backslash galaxies (Diemer & Kravtsov 2014; Adhikari et al. 2014; More et al. 2015, 2016; Mansfield et al. 2017; O’Neil et al. 2021; Borrow et al. 2023) now in the field that were environmentally heated by their interactions with massive groups or clusters. We trace the distance of these three ETGs to all the more massive FoF groups it historically belonged to and how their temperatures evolved in the same period ($0 < z < 1$) along their main progenitor branches of their merger trees. For tracing gas temperature, we adopt the mass-weighted temperature definition following Bartelmann & Steinmetz (1996); Mathiesen & Evrard (2001):

$$T_{\text{mw}} = \frac{\sum_i m_i T_i}{\sum_i m_i}, \quad (2)$$

where m_i and T_i are the mass and temperature of the i -th gas cell. The reason why we choose T_{mw} over T_{sl} for temperature tracing is that, in the event of shock heating (from falling into a more massive halo), the heated cells lose weight rapidly due to the $T^{-3/4}$ scaling in the T_{sl} definition. This dials down the effect of heating as measured by T_{sl} , while the mass-weighted temperature T_{mw} is not sensitive to the gas cell temperature. There is also better physical motivation to trace the mass-weighted temperature, as the total internal energy of the gas

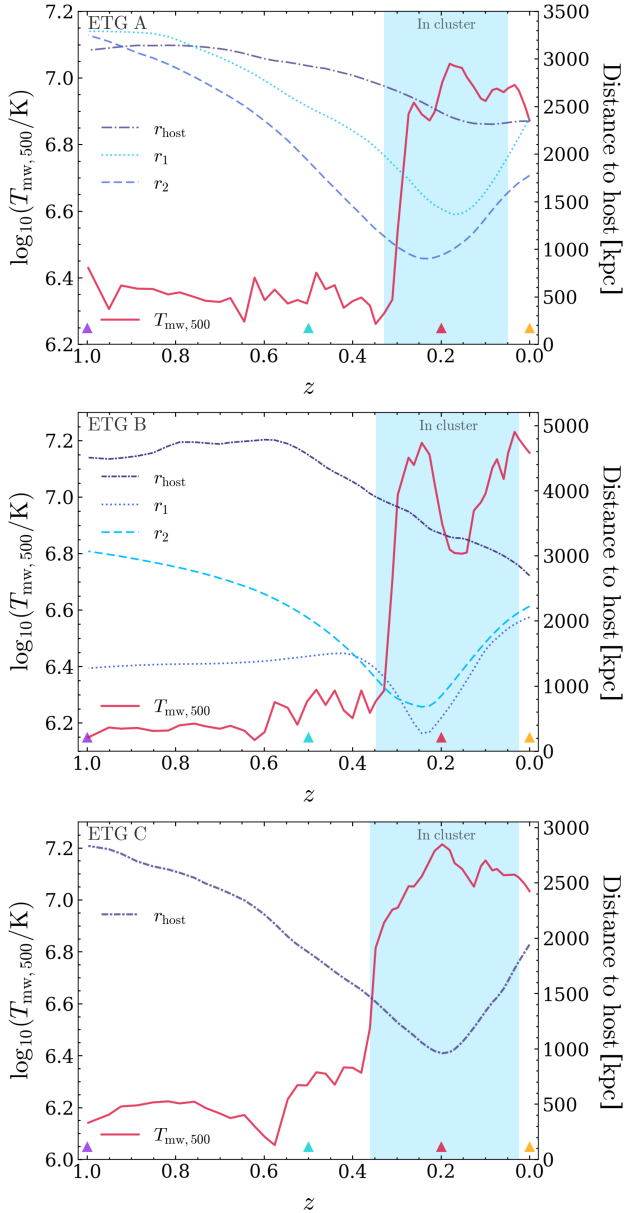


Figure 5. This figure shows the mass-weighted temperature history and distances to host haloes they interacted with for the three outlier ETGs in Fig. 2. In each panel, the mass-weighted temperature tracks are denoted by the solid red curve and refers to the left y-axis ($T_{\text{mw},500}$). The distances to the host FoF groups (r_{host}) and other major subhaloes (r_1 , r_2 for ETGs A and B) they interacted with are indicated by the blue curves that refer to the right y-axis. The blue shaded region in each panel indicates the period when each ETG was inside the larger cluster they interacted with. The colored triangles stand for the four redshifts $z = 0, 0.2, 0.5, 1$ at which we show temperature maps in Fig. 6 and gas temperature and density profiles in Fig. 7.

$U \propto mT_{\text{mw}}$ and reflects the energetic state of the gas in the CGM. Similar to the T_{sl} definition in Section 2.3, we also neglect the very cold and dense gas cells with temperature $T_i < 0.05$ keV ($\sim 5.8 \times 10^5$ K), number density $n_{\text{H},i} > 0.1$, or star formation rate $\text{SFR} > 0$ when calculating T_{mw} . We show a comparison in Appendix C between the spectroscopic-like temperature and mass-weighted temperature

for all 559 ETGs in our sample. The $T_{\text{mw},500}$ definition yields ~ 0.2 dex higher temperatures than the $T_{\text{sl},500}$ definition for our ETGs.

4.1 Temperature history and interactions with larger clusters

In Fig. 5, we show the $T_{\text{mw},500}$ evolution history for the three outlier ETGs from $z = 1$ to $z = 0$. Their gas mass-weighted temperatures all seem to jump up at $z \sim 0.35$. By examining their merger trees and cluster (FoF group) memberships, we find that they all belonged to a much larger cluster during the periods indicated by the vertical dashed lines in each panel. They all interacted with larger galaxy groups/clusters since $z \sim 0.35$, lost their central ETG identity during their infall, and came back to become backsplash centrals just before $z = 0$.

We also show their distances to the host FoF group and major subhaloes of those clusters (subhaloes by $z = 0$) that they interacted with as a function of time (blue curves, right y-axis in Fig. 5). The temperature rise of each ETG coincides well with their first accretion into a larger cluster, and temperature peaks correspond to the closest encounters with the brightest cluster galaxy (BCG) or other member galaxies, indicative of environmental heating of their gas. To further demonstrate this process, we plot the mass-weighted temperature maps at $z = 1, 0.5, 0.2, 0$ in the surroundings of each ETG in Fig. 6. We only include gas cells associated with the ETGs and the larger cluster they interacted with in these temperature maps. We analyze how the three ETG formation histories impact the heating of their gas on a case-by-case basis:

- ETG A (SUBFIND ID 410700) interacted with parts of a FoF group that has a $z = 0$ $\log_{10}(M_{200}/M_{\odot}) = 13.95$. Specifically, it mainly interacted with two subhaloes of the host FoF group, the first one (r_1) having a $z = 0$ total mass of $\log_{10}(M_{\text{sub}}/M_{\odot}) = 13.44$, and the second one (r_2) having a $z = 0$ total mass of $\log_{10}(M_{\text{sub}}/M_{\odot}) = 13.02$. The two temperature peaks of the ETG at $z \sim 0.25$ and $z \sim 0.2$ coincide well with the pericentric passages with these two subhaloes, after which the gas in the ETG remained ~ 0.7 dex hotter than pre-infall. From the temperature maps we can see that the ETG (white squares) started interacting with outskirt gas in subhalo r_2 at $z = 0.5$, heated up and remained to be surrounded by extended hot gas from the host halo of the larger FoF group even after exiting at $z = 0$.

- ETG B (SUBFIND ID 482814) interacted with the largest cluster in TNG100, which has a $z = 0$ $\log_{10}(M_{200}/M_{\odot}) = 14.58$. It first interacted with two subhaloes of the cluster, the first one (r_1) having a $z = 0$ total mass of $\log_{10}(M_{\text{sub}}/M_{\odot}) = 13.06$, and the second one (r_2) having a $z = 0$ total mass of $\log_{10}(M_{\text{sub}}/M_{\odot}) = 12.48$. The ETG hit pericenter with these two subhaloes almost at the same time of $z \sim 0.25$, corresponding to the first temperature peak after which the gas starts to cool. The second peak towards $z = 0$ in the temperature history comes from the final approach of the ETG onto the most massive cluster, when the other two subhaloes already finished their infall. Although the ETG is a central galaxy of a individual FoF group at $z = 0$, it is in a multi-merger series happening in the densest region of the box and is impacted by the extremely hot and extended gas of the largest cluster in the simulation.

- ETG C (SUBFIND ID 486341) interacted directly with the host halo of a FoF group that has a $z = 0$ $\log_{10}(M_{200}/M_{\odot}) = 14.32$. Again, the gas temperature in the ETG starts to rise rapidly after becoming part of the larger FoF group, and its temperature peak at $z \sim 0.2$ corresponds well to the pericenter passage with the host halo. After exiting the FoF group at $z = 0.02$, the ETG still submerges in

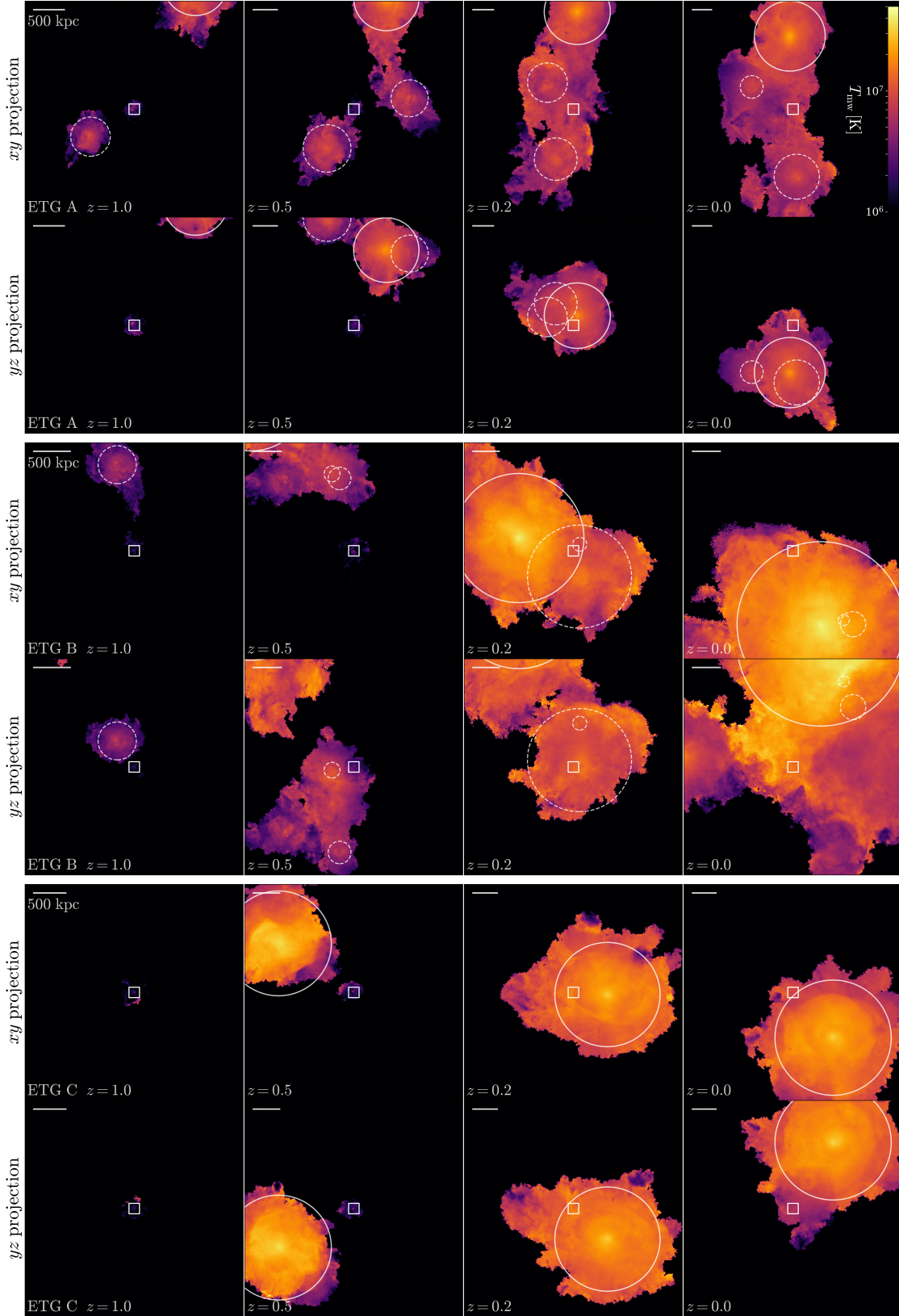


Figure 6. The projected mass-weighted temperature maps at $z = 1, 0.5, 0.2, 0$ for ETG A (top panel), B (middle panel), and C (bottom panel) and the large clusters they interacted with. In each panel, the top row shows the gas temperature in the x - y plane while the bottom row in the y - z plane, with both rows taking the y -axis in the horizontal direction. ETGs A, B, and C in each subplot are fixed in the center (white squares); the cluster host halo R_{200} are marked by solid white circles; the $2\times$ stellar-half-mass radius of the subhalos with which these three ETGs interacted with are marked by dashed white circles. The scale bars in the top left corner of each temperature maps stand for 500 physical kpc. The color map for all subplots range from 10^6 K to $10^{7.7}$ K as shown in the top right corner. These gas temperature maps further elucidate the context of environmental heating for the three outlier ETGs.

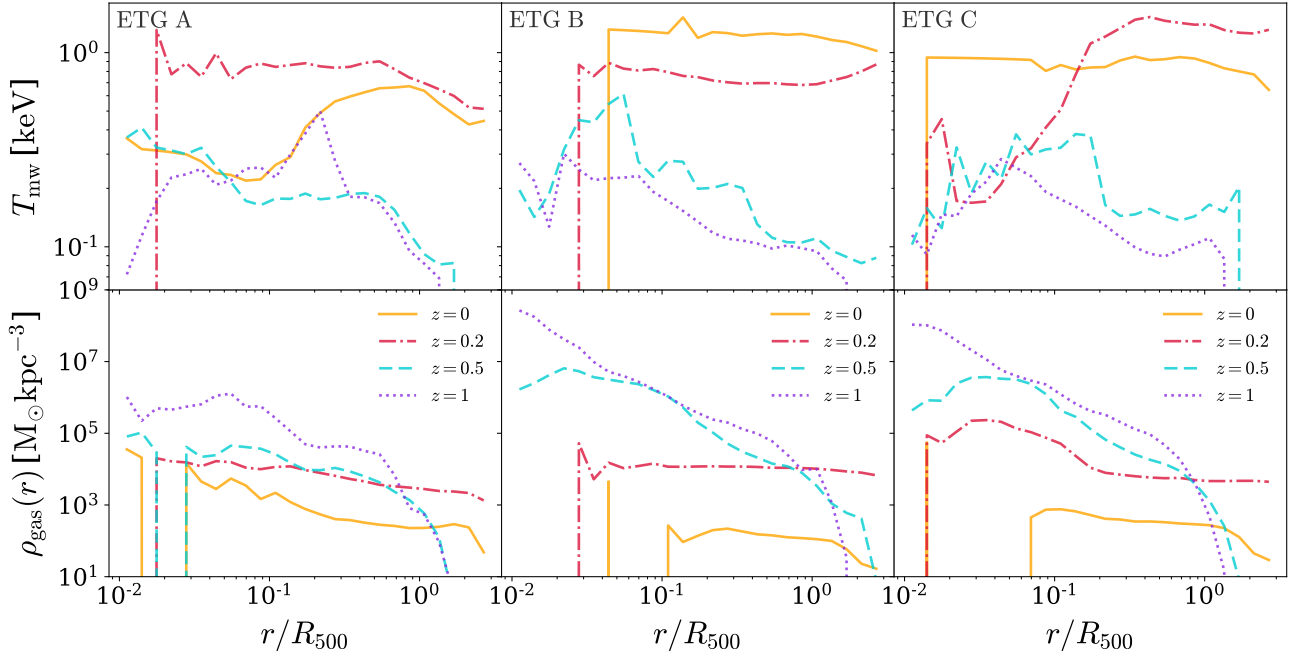


Figure 7. The gas mass-weighted temperature (top row) and gas density (bottom row) profiles within $3 \times R_{500}$ for the three outlier ETGs we studied in Fig. 6, with each column showing one galaxy. The R_{500} values are for the host haloes of the three ETGs at $z = 0$, $z = 0.5$, and $z = 1$ when they were the central galaxies. We take the average value of the pre-infall and post-infall R_{500} of the ETG as their approximate R_{500} at $z = 0.2$. The four sets of curves in each row indicate the gas temperature and density profiles at four different redshifts, i.e. $z = 0, 0.2, 0.5, 1$. These four redshifts correspond to the epochs shown in Fig. 6, which cover before entering, right within, and after exiting the more massive clusters each ETG interacted with. Through these interactions, the temperature profiles develop very hot outskirts and the gas density becomes very sparse.

the extended hot gas of the cluster and maintains ~ 0.8 dex higher gas temperature than its pre-interaction temperature.

These three case studies clearly demonstrate that the outliers in the L_X-T_{sl} relation originate from environmental heating of the hot gas through interactions with larger galaxy clusters. Since they are back-splash ETGs that are relatively low in mass, their change in potential energy are insufficient to cause the order-of-magnitude increase in temperature due to gravitational heating. The presence of a virial shock (Birnbom & Dekel 2003) in the host halo can heat the accreted gas to the virial temperature of the host halo. Although some of the encounters above do not penetrate deep into the halo, we find that the extended gas outside of R_{200} of the larger clusters these ETGs interacted can still have much higher temperatures that supports external heating (Kim et al. 2020). Although observers (Goulding et al. 2016) did not find significant temperature differences for ETGs in cluster/group versus field environments, indicating that environmental heating may not impact the ‘main ridge’ of the L_X-T_{sl} relation, shock heating and ram-pressure compression can still work in special circumstances as in our three outlier ETGs that heat up the remaining gas during merger interactions.

For massive $M_* > 10^{10} M_\odot$ galaxies experiencing tidal interactions in IllustrisTNG, Li et al. (2022) found that the ISM ($r \in [0, 2R_e]$) and CGM ($r \in [2R_e, 4R_e]$) can get stripped by $\geq 70\%$ in the absence of shocks and $\geq 90\%$ with shocks, leading to significant removal of the total gas content. Indeed, in Fig. 2 left panel, the L_X of these three outlier ETGs is all below the best-fit $L_{X,500}-M_{500}$ relation, indicating gas stripping in all three cases. Therefore, the combination of environmental heating raising T_{sl} and tidal/ram-pressure stripping lowering L_X (removing gas content) during these

mergers/interactions with larger clusters lead to these significant outliers of the L_X-T_{sl} scaling relations.

Through visually examining the gas temperature and FoF group membership history of each ETG in our sample, we found *four* other ETGs that similarly had encounters with more massive FoF groups but lie on the main sequence of the L_X-T_{sl} scaling relation. We find that three of these four ‘normal’ ETGs had very large M_{500} mass ratios ($> 1/2$) with their host halos and their gas temperatures only increased ~ 0.3 dex during these interactions. The remaining ‘normal’ ETG interacted with a massive cluster with $M_{500} \sim 10^{13.7} M_\odot$ towards $z = 0$, which should have made it an outlier ETG in the L_X-T_{sl} plane as with ETGs A, B, and C. However, this ETG was only part of the larger FoF group for ≤ 1 Gyr and brushed the cluster outskirts (> 2.8 Mpc), rendering the environmental heating from the host ineffective. Therefore, back-splash ETGs need to have close interactions with massive clusters ($M_{500} \sim 10^{14} M_\odot$) in order to be detectable as L_X-T_{sl} scaling relation outliers.

4.2 Gas temperature and density profiles

To elaborate on the scenario described above, we further show in Fig. 7 the mass-weighted temperature and density profiles of gas for the three outlier ETGs at $z = 0, 0.2, 0.5, 1$. In these profiles, we use all gas particles that are enclosed within $3R_{500}$ of the ETG host halos at that redshift (for $z = 0.2$ when these ETGs were in larger FoF groups and their own R_{500} could not be defined, we use the average value of their pre-infall and post-infall R_{500} values). The triangles in Fig. 6 mark these epochs and correspond to times before infall, while within, and just after exiting the more massive FoF groups each of these ETGs interacted with.

At $z = 1$ and $z = 0.5$ before entering the larger clusters they

interacted with, ETG A has an overall flat mass-weighted temperature profile within R_{500} , while ETGs B and C have decreasing temperature profiles with increasing radius. The density profiles show that all three ETGs started out with cuspy gas profiles at $z = 1$ (especially ETG B and C) within $r \sim 0.1R_{500}$ and the outer density profiles follow steep power-law-shaped profiles.

At $z = 0.2$ when these three ETGs were within larger FoF groups, their temperature profiles are significantly boosted. For ETG A, the temperature profile is almost flat and everywhere hotter than before infall. Most of the gas in ETG B also has a hot and flat temperature profile at $z = 0.2$, and even a small rise in temperature beyond R_{500} . This is a clear signature for the onset of external heating (Kim et al. 2020) due to the interactions. External heating is again most evident in ETG C, where the gas within $r \lesssim 0.03R_{500}$ still has similar temperatures with pre-infall ($z = 0.5$), while the gas temperature significantly rises from $0.03R_{500}$ to $0.2R_{500}$, beyond which the gas temperature is much hotter and flat with radius. The density profiles show unanimous boosting of the outer gas density in all three ETGs at $z = 0.2$ at $r \gtrsim 0.5R_{500}$. Comparing the spatial extent of the hot gas of the larger FoF groups these ETGs interacted with in Fig. 6, the much hotter gas in the larger clusters is almost a constant background medium to these ETGs during the interactions. The gas density in the core region ($r \lesssim 0.1R_{500}$) for all three ETGs decrease as compared to $z = 0.5$, indicative of external (shock) heating and gas stripping.

Finally at $z = 0$, when these three ETGs splashed-back from the larger FoF groups and became BCGs of their own groups, they all show significantly sparser gas density profiles compared to that before infall or during the interactions. Cooling in the center of ETG A leads to a flat cooler core and rising temperature at the outskirts, preserving signatures of environmental heating. The temperature profiles for ETG B and C both are hot and flat at $z = 0$. The former (ETG B) has a final temperature higher than the $z = 0.2$ temperature profile as it is starting its final approach onto the largest cluster in the TNG100 box at $z = 0$ and keeps heating up (also see Fig. 6, middle row). The outskirts of the latter (ETG C) has a cooler temperature at $z = 0$ than during the interaction at $z = 0.2$ as the gas starts to cool after exiting the large cluster.

These gas temperature and density profiles further support the environmental heating scenario described in Section 4.1 as the cause of them being significant outliers in the L_X-T_{sl} scaling relation. We argue that similar outliers seen in observed ETG X-ray scaling relations are also backplash objects that might have recently had their gas heated up environmentally. This finding can also potentially facilitate systematic searches of backplash objects around the outskirts of large galaxy clusters using next generation X-ray telescopes (e.g., eROSITA Merloni et al. 2012, Athena+ Nandra et al. 2013, Lynx Gaskin et al. 2019 etc.) by looking for outliers in the L_X-T_{sl} scaling relation. The three outlier ETGs we investigated all fell into massive clusters at $z \sim 0.35$ and became backplash galaxies at $z = 0$. This coincides well with the $2\times$ dynamical timescale for dark matter halos at $z = 0$ which is 3.89 Gyrs ($z = 0.37$). Therefore, we expect these environmentally heated ETGs to stand out as outliers on the L_X-T_{sl} relation for approximately two dynamical timescales at their respective redshifts. Future work combining redshift-dependent halo merger rates with subhalo pericenter distance distributions could yield quantitative forecasts for the detection rate of backplash ETGs in upcoming X-ray surveys.

5 CONCLUSIONS

In this paper, we have explored the X-ray scaling relations of hot gas in massive ETGs from IllustrisTNG-100. We derived mock X-ray luminosities (using the public code MOCK-X) and spectroscopic-like temperatures for a legacy mock-ETG sample from Wang et al. (2020) that has well-studied total density profiles and dark matter fractions. We compared the X-ray luminosity-mass relation and the X-ray luminosity-temperature relation to observations for the simulated ETGs. We further studied how the low-mass end scatter in the X-ray luminosity-mass scaling relation relates to the ETG dark matter fraction, gas fraction, stellar population, and AGN feedback activities. Our major findings are as follows:

- (i) The $L_{X,500}-M_{5R_c}$ scaling relation has a very similar slope and overall scatter to the observed Chandra ETGs. The scatter increases at the low-mass end compared to the high-mass end. The $L_{X,500}-T_{\text{sl},500}$ scaling relation has slightly steeper slope than the observed Chandra ETGs, though hot gas in IllustrisTNG ETGs are on average ~ 0.5 dex cooler than observations (Fig. 2).
- (ii) We do not observe significant correlation between $L_{X,500}$ and the ETG dark matter fraction (including the small amount of gas) $1 - f_{\text{star}}$ at the low-mass end (Fig. 3 left). The offset from the best-fit X-ray luminosity-mass relation $\Delta L_{X,500}$ negatively correlates with $1 - f_{\text{star}}$ similar to observations (Fig. 3 right), although IllustrisTNG ETGs have systematically larger dark matter fractions than observations, which was already known in earlier literature.
- (iii) At the low-mass end ($\log_{10}(M_{5R_c}/M_{\odot}) \leq 11.5$) ETGs that up-scatter in $L_{X,500}$ (vice versa the following for down-scatter) tend to have higher gas fractions and younger stellar populations. This is caused by their AGN having lower cumulative kinetic feedback energy, which leads to their higher gas content and less efficient quenching. As a consequence, the younger stars could also provide stronger stellar feedback heating that further increases L_X . The higher gas fraction in the end fuels more active recent black hole accretion, leading to these up-scatter ETGs having stronger recent ($z < 0.1$) AGN kinetic feedback (Fig 4).
- (iv) Past AGN feedback mediates star formation and stellar populations in ETGs, thereby influencing the strength of stellar feedback at present-day. This can partially explain why observations see a sub-dominant role of AGN compared to stellar feedback with only access to $z = 0$ AGN properties and not their full accretion history (Section 3.3).
- (v) The scatter of $L_{X,500}$ does not correlate with the total density profiles of the ETGs at the low mass end. This indicates that mergers, which dominate the ETG density profile evolution at $z \lesssim 1$, do not significantly impact $L_{X,500}$ at fixed M_{5R_c} (Figs. 3, 4).

We also investigated the merger histories of three individual ETGs (Fig. 2 black squares) that are outliers of the X-ray luminosity-temperature scaling relation. We find that:

- (i) All three ETGs interacted with much larger galaxy groups/clusters since $z \sim 0.4$ and were environmentally heated. Their gas temperature rise coherently with their infall into these larger FoF groups, and the temperature peaks coincide well with pericenter passages with those larger galaxy clusters (Fig. 6). Their gas temperature and density profiles also show clear signatures of external heating, leaving those ETGs with very sparse and hot gas atypical of their mass at $z = 0$ (Fig. 7).
- (ii) Given that the three outlier ETGs are backplash galaxies, we propose that querying outliers of the L_X-T_{sl} relation can potentially be used as a search strategy for backplash ETGs near galaxy clusters.

As a final note, AGN feedback impacting the scatter in the low-mass-end of the $L_{X,500}-M_{5R_e}$ relation can be regarded as a theoretical prediction that could be verified in future observations correlating X-ray gas to the AGN of ETGs. New observations will provide important constraints for developing more realistic AGN feedback models in hydrodynamic simulations (e.g. more measurements for the stellar ages of low-mass X-ray ETGs) and testing the picture we have developed. As for finding backplash objects using outliers in the L_X-T_{sl} relation, future X-ray missions can target the outskirts of galaxy clusters for red galaxies (cross-correlating with optical surveys) that simultaneously possess a hot X-ray component. Care should be taken as the signal-to-noise of such searches may be limited to the specific instrument and the success of the proposed backplash search campaign depends on the sensitivity to the contrast between the backplash ETG gas and the extend hot gas from the large galaxy cluster. Nonetheless, our work here still provides a promising novel approach to finding backplash galaxies in addition to the existing density profile-based (Adhikari et al. 2021) or surface-brightness-fluctuation-based (Casey et al. 2022) inference methods that could yield fruitful outcomes in the near future.

ACKNOWLEDGEMENTS

We would like to acknowledge the past contributions of David Barnes to this paper before a career shift beyond astronomy. We thank Ethan Nadler, Hui Li, Phil Mansfield, Risa Wechsler, and Shy Genel for helpful discussions and comments while preparing this draft. YW acknowledges the support of a Stanford-KIPAC Chabolla Fellowship. MV acknowledges support through NASA ATP 19-ATP19-0019, 19-ATP19-0020, 19-ATP19-0167, and NSF grants AST-1814053, AST-1814259, AST-1909831, AST-2007355 and AST-2107724. This research made use of computational resources at the MIT and Harvard research computing facilities supported by FAS and MIT MKI; the authors are thankful for the support from the FAS Research Computing and MIT Engaging technical teams. The flagship simulations of the IllustrisTNG project used in this work have been run on the HazelHen Cray XC40-system at the High Performance Computing Center Stuttgart as part of project GCS-ILLU of the Gauss Centre for Supercomputing (GCS). This research made extensive use of [arXiv.org](https://arxiv.org) and NASA's Astrophysics Data System for bibliographic information.

REFERENCES

- Abbott T. M. C., et al., 2018, *Phys. Rev. D*, **98**, 043526
- Adhikari S., Dalal N., Chamberlain R. T., 2014, *J. Cosmology Astropart. Phys.*, **2014**, 019
- Adhikari S., et al., 2021, *ApJ*, **923**, 37
- Alabi A. B., et al., 2017, *MNRAS*, **468**, 3949
- Allen S. W., Evrard A. E., Mantz A. B., 2011, *ARA&A*, **49**, 409
- Auger M. W., Treu T., Bolton A. S., Gavazzi R., Koopmans L. V. E., Marshall P. J., Moustakas L. A., Burles S., 2010, *ApJ*, **724**, 511
- Babyk I. V., McNamara B. R., Nulsen P. E. J., Hogan M. T., Vantyghem A. N., Russell H. R., Pulido F. A., Edge A. C., 2018, *ApJ*, **857**, 32
- Barnabè M., Czoske O., Koopmans L. V. E., Treu T., Bolton A. S., 2011, *MNRAS*, **415**, 2215
- Barnes D. J., et al., 2018, *MNRAS*, **481**, 1809
- Barnes D. J., Vogelsberger M., Pearce F. A., Pop A.-R., Kannan R., Cao K., Kay S. T., Hernquist L., 2021, *MNRAS*, **500**, 431
- Bartelmann M., Steinmetz M., 1996, *MNRAS*, **283**, 431
- Bellstedt S., et al., 2018, *MNRAS*, **476**, 4543
- Birnboim Y., Dekel A., 2003, *MNRAS*, **345**, 349
- Bleem L. E., et al., 2015, *ApJS*, **216**, 27
- Borison B., Kim D.-W., Fabbiano G., 2011, *ApJ*, **729**, 12
- Borrow J., Vogelsberger M., O'Neil S., McDonald M. A., Smith A., 2023, *MNRAS*, **520**, 649
- Bruzual G., Charlot S., 2003, *MNRAS*, **344**, 1000
- Bryan G. L., Norman M. L., 1998, *ApJ*, **495**, 80
- Cappellari M., et al., 2011, *MNRAS*, **416**, 1680
- Casey K. J., Greco J. P., Peter A. H. G., Davis A. B., 2022, arXiv e-prints, p. arXiv:2211.00629
- Ceverino D., Klypin A., 2009, *ApJ*, **695**, 292
- Choi E., Ostriker J. P., Naab T., Oser L., Moster B. P., 2015, *MNRAS*, **449**, 4105
- Ciotti L., Pellegrini S., Negri A., Ostriker J. P., 2017, *ApJ*, **835**, 15
- Croton D. J., et al., 2006, *MNRAS*, **365**, 11
- David L. P., Jones C., Forman W., Vargav I. M., Nulsen P., 2006, *ApJ*, **653**, 207
- Derkenne C., McDermid R. M., Poci A., Remus R.-S., Jørgensen L., Emsellem E., 2021, *MNRAS*, **506**, 3691
- Di Matteo T., Springel V., Hernquist L., 2005, *Nature*, **433**, 604
- Diemer B., Kravtsov A. V., 2014, *ApJ*, **789**, 1
- Dolag K., Borgani S., Murante G., Springel V., 2009, *MNRAS*, **399**, 497
- Donnari M., et al., 2019, *MNRAS*, **485**, 4817
- Donnari M., et al., 2021, *MNRAS*, **500**, 4004
- Eisenstein D. J., et al., 2011, *AJ*, **142**, 72
- Etherington A., et al., 2022, arXiv e-prints, p. arXiv:2207.04070
- Fabian A. C., 2012, *ARA&A*, **50**, 455
- Forbes D. A., Alabi A., Romanowsky A. J., Kim D.-W., Brodie J. P., Fabbiano G., 2017, *MNRAS*, **464**, L26
- Foster A. R., Ji L., Smith R. K., Brickhouse N. S., 2012, *ApJ*, **756**, 128
- Gaskin J. A., et al., 2019, *Journal of Astronomical Telescopes, Instruments, and Systems*, **5**, 021001
- Genel S., et al., 2014, *MNRAS*, **445**, 175
- Genel S., et al., 2018, *MNRAS*, **474**, 3976
- Goulding A. D., et al., 2016, *ApJ*, **826**, 167
- Habouzit M., et al., 2019, *MNRAS*, **484**, 4413
- Harris W. E., Harris G. L. H., Alessi M., 2013, *ApJ*, **772**, 82
- Harris W. E., Blakeslee J. P., Harris G. L. H., 2017, *ApJ*, **836**, 67
- Hemler Z. S., et al., 2021, *MNRAS*, **506**, 3024
- Hilton M., et al., 2018, *ApJS*, **235**, 20
- Hoekstra H., Herbonnet R., Muzzin A., Babul A., Mahdavi A., Viola M., Cacciato M., 2015, *MNRAS*, **449**, 685
- Kauffmann G., Nelson D., Borthakur S., Heckman T., Hernquist L., Marinacci F., Pakmor R., Pillepich A., 2019, *MNRAS*, **486**, 4686
- Kim D.-W., Fabbiano G., 2013, *ApJ*, **776**, 116
- Kim D.-W., Fabbiano G., 2015, *ApJ*, **812**, 127
- Kim D.-W., et al., 2019a, *ApJS*, **241**, 36
- Kim D.-W., James N., Fabbiano G., Forbes D., Alabi A., 2019b, *MNRAS*, **488**, 1072
- Kim D.-W., et al., 2020, *MNRAS*, **492**, 2095
- Kormendy J., Fisher D. B., Cornell M. E., Bender R., 2009, *ApJS*, **182**, 216
- Kravtsov A. V., Borgani S., 2012, *ARA&A*, **50**, 353
- Lee E., et al., 2022, *MNRAS*, **517**, 5303
- Li H., Wang H., Mo H. J., Wang Y., Luo X., Li R., 2022, arXiv e-prints, p. arXiv:2209.07711
- Lovell M. R., et al., 2018, *MNRAS*, **481**, 1950
- Ma C.-P., Greene J. E., McConnell N., Janish R., Blakeslee J. P., Thomas J., Murphy J. D., 2014, *ApJ*, **795**, 158
- Mansfield P., Kravtsov A. V., Diemer B., 2017, *ApJ*, **841**, 34
- Mantz A., Allen S. W., Rapetti D., Ebeling H., 2010a, *MNRAS*, **406**, 1759
- Mantz A., Allen S. W., Ebeling H., Rapetti D., Drlica-Wagner A., 2010b, *MNRAS*, **406**, 1773
- Mantz A. B., et al., 2015, *MNRAS*, **446**, 2205
- Mantz A. B., et al., 2016, *MNRAS*, **463**, 3582
- Marinacci F., et al., 2018, *MNRAS*, **480**, 5113
- Mathiesen B. F., Evrard A. E., 2001, *ApJ*, **546**, 100
- Mazzotta P., Rasia E., Moscardini L., Tormen G., 2004, *MNRAS*, **354**, 10
- Merloni A., et al., 2012, arXiv e-prints, p. arXiv:1209.3114
- More S., Diemer B., Kravtsov A. V., 2015, *ApJ*, **810**, 36

More S., et al., 2016, *ApJ*, **825**, 39
 Naiman J. P., et al., 2018, *MNRAS*, **477**, 1206
 Nandra K., et al., 2013, arXiv e-prints, p. arXiv:1306.2307
 Nelson D., et al., 2015, *Astronomy and Computing*, **13**, 12
 Nelson D., et al., 2018, *MNRAS*, **475**, 624
 Nelson D., et al., 2019a, *Computational Astrophysics and Cosmology*, **6**, 2
 Nelson D., et al., 2019b, *MNRAS*, **490**, 3234
 Nelson E. J., et al., 2021, *MNRAS*, **508**, 219
 Neto A. F., et al., 2007, *MNRAS*, **381**, 1450
 O’Neil S., Barnes D. J., Vogelsberger M., Diemer B., 2021, *MNRAS*, **504**, 4649
 O’Sullivan E., Forbes D. A., Ponman T. J., 2001, *MNRAS*, **328**, 461
 O’Sullivan E., Ponman T. J., Collins R. S., 2003, *MNRAS*, **340**, 1375
 Oppenheimer B. D., et al., 2020, *ApJ*, **893**, L24
 Pellegrini S., 1999, *A&A*, **351**, 487
 Pellegrini S., 2011, *ApJ*, **738**, 57
 Pillepich A., et al., 2018a, *MNRAS*, **473**, 4077
 Pillepich A., et al., 2018b, *MNRAS*, **475**, 648
 Pillepich A., et al., 2019, *MNRAS*, **490**, 3196
 Piotrowska J. M., Bluck A. F. L., Maiolino R., Peng Y., 2022, *MNRAS*, **512**, 1052
 Planck Collaboration et al., 2016a, *A&A*, **594**, A13
 Planck Collaboration et al., 2016b, *A&A*, **594**, A27
 Poci A., Cappellari M., McDermid R. M., 2017, *MNRAS*, **467**, 1397
 Pop A.-R., et al., 2022, arXiv e-prints, p. arXiv:2205.11528
 Remus R.-S., Dolag K., Naab T., Burkert A., Hirschmann M., Hoffmann T. L., Johansson P. H., 2017, *MNRAS*, **464**, 3742
 Rodriguez-Gomez V., et al., 2019, *MNRAS*, **483**, 4140
 Ruff A. J., Gavazzi R., Marshall P. J., Treu T., Auger M. W., Brault F., 2011, *ApJ*, **727**, 96
 Rykoff E. S., et al., 2014, *ApJ*, **785**, 104
 Rykoff E. S., et al., 2016, *ApJS*, **224**, 1
 Sarzi M., et al., 2013, *MNRAS*, **432**, 1845
 Shajib A. J., Treu T., Birrer S., Sonnenfeld A., 2021, *MNRAS*, **503**, 2380
 Sijacki D., Vogelsberger M., Genel S., Springel V., Torrey P., Snyder G. F., Nelson D., Hernquist L., 2015, *MNRAS*, **452**, 575
 Smith R. K., Brickhouse N. S., Liedahl D. A., Raymond J. C., 2001, *ApJ*, **556**, L91
 Sonnenfeld A., Treu T., Gavazzi R., Suyu S. H., Marshall P. J., Auger M. W., Nipoti C., 2013, *ApJ*, **777**, 98
 Springel V., 2010, *MNRAS*, **401**, 791
 Springel V., Hernquist L., 2003, *MNRAS*, **339**, 289
 Springel V., White S. D. M., Tormen G., Kauffmann G., 2001, *MNRAS*, **328**, 726
 Springel V., Di Matteo T., Hernquist L., 2005, *MNRAS*, **361**, 776
 Springel V., et al., 2018, *MNRAS*, **475**, 676
 Terrazas B. A., et al., 2020, *MNRAS*, **493**, 1888
 Thomas J., Saglia R. P., Bender R., Thomas D., Gebhardt K., Magorrian J., Corsini E. M., Wegner G., 2007, *MNRAS*, **382**, 657
 Torrey P., Vogelsberger M., Genel S., Sijacki D., Springel V., Hernquist L., 2014, *MNRAS*, **438**, 1985
 Torrey P., et al., 2018, *MNRAS*, **477**, L16
 Torrey P., et al., 2019, *MNRAS*, **484**, 5587
 Tortora C., La Barbera F., Napolitano N. R., Romanowsky A. J., Ferreras I., de Carvalho R. R., 2014, *MNRAS*, **445**, 115
 Truong N., et al., 2020, *MNRAS*, **494**, 549
 Truong N., Pillepich A., Werner N., 2021, *MNRAS*, **501**, 2210
 Vikhlinin A., et al., 2009, *ApJ*, **692**, 1033
 Vogelsberger M., Genel S., Sijacki D., Torrey P., Springel V., Hernquist L., 2013, *MNRAS*, **436**, 3031
 Vogelsberger M., et al., 2014a, *MNRAS*, **444**, 1518
 Vogelsberger M., et al., 2014b, *Nature*, **509**, 177
 Vogelsberger M., et al., 2018, *MNRAS*, **474**, 2073
 Vogelsberger M., Marinacci F., Torrey P., Puchwein E., 2020a, *Nature Reviews Physics*, **2**, 42
 Vogelsberger M., et al., 2020b, *MNRAS*, **492**, 5167
 Wang Y., et al., 2019, *MNRAS*, **490**, 5722
 Wang Y., et al., 2020, *MNRAS*, **491**, 5188

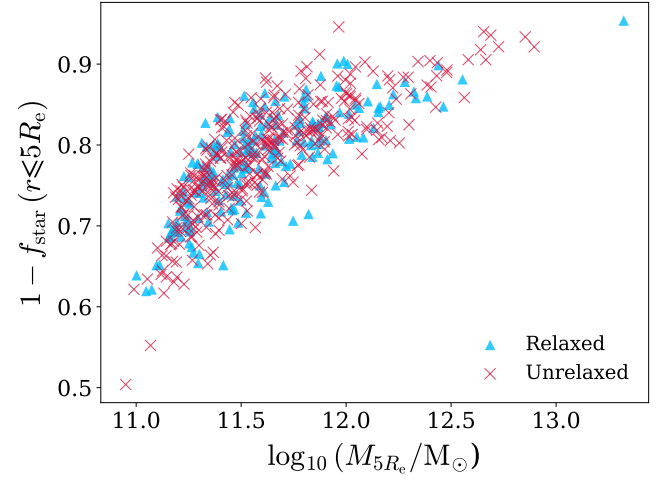


Figure A1. The dark matter fraction ($1 - f_{\text{star}}$) versus the total mass within $5R_e$. The blue triangles indicate galaxies that occupy relaxed haloes, while the red crosses indicate unrelaxed host haloes. See Section A for the definition of relaxation. There are no significant differences in the dark matter fraction of relaxed and unrelaxed ETG haloes.

Wang Y., Mao S., Vogelsberger M., Springel V., Hernquist L., Wechsler R. H., 2022, *MNRAS*, **513**, 6134
 Weinberger R., et al., 2017, *MNRAS*, **465**, 3291
 Weinberger R., et al., 2018, *MNRAS*, **479**, 4056
 Weinberger R., Springel V., Pakmor R., 2020, *ApJS*, **248**, 32
 White Raymond E. I., Sarazin C. L., 1991, *ApJ*, **367**, 476
 Wojtak R., Mamon G. A., 2013, *MNRAS*, **428**, 2407
 Xu D., Springel V., Sluse D., Schneider P., Sonnenfeld A., Nelson D., Vogelsberger M., Hernquist L., 2017, *MNRAS*, **469**, 1824
 Xu D., et al., 2019, *MNRAS*, **489**, 842
 Zinger E., et al., 2020, *MNRAS*, **499**, 768
 von der Linden A., et al., 2014, *MNRAS*, **439**, 2

APPENDIX A: DYNAMICAL STATE OF THE ETG HOST HALOES

In Fig. A1, we show the dark matter fraction ($1 - f_{\text{star}}(\leq 5R_e)$) versus the total mass of the central ETGs within $5R_e$. The scattered dots are divided into two populations, where one denotes galaxies that occupy relaxed haloes (blue triangles), and the other denotes galaxies that live in unrelaxed ones (red crosses). The definition for relaxed haloes is adopted from Neto et al. (2007):

$$|\mathbf{r}_{\text{pos}} - \mathbf{r}_{\text{CM}}| \leq 0.07R_{200}, \quad (\text{A1})$$

where \mathbf{r}_{pos} is the location of the deepest-potential particle identified in the simulation by SUBFIND, \mathbf{r}_{CM} is the center of mass for all particles within the FoF group, and R_{200} is the physical radius within which the average density of the halo is 200 times that of the critical density of the universe. Our sample includes relaxed and unrelaxed haloes in comparable amounts according to this definition, and that they do not show significant differences in the dark matter fraction/total mass space. Hence, the dynamical state of the host halo for our ETGs should have an insignificant impact on our analysis.

APPENDIX B: BLACK HOLE MASS AND THERMAL AGN FEEDBACK EFFECTS ON THE LUMINOSITY-MASS SCALING RELATION

In this appendix we present the insignificant impact of SMBH mass and radiative mode AGN feedback energy on the scatter of the $L_{X,500}$ – M_{5R_e} scaling relation at the low-mass end. In Fig. B1, we show the $L_{X,500}$ – M_{5R_e} scaling relation colored by the SMBH mass (M_{BH} , top panel), cumulative thermal AGN feedback energy ($\Sigma E_{\text{AGN,Thm}}$, middle panel), and the recent AGN thermal feedback energy from $z = 0.1$ to $z = 0$ ($\delta E_{\text{AGN,Thm}}$, bottom panel). In each panel, we also include insets that further illustrate the correlation between the colored physical quantities and $\Delta L_{X,500}$ for low-mass ETGs with $\log_{10}(M_{5R_e}/M_{\odot}) \leq 11.5$. Through the color maps in the main scaling relations large Pearson p values for the linear fits in the inset plots, we conclude that none of the three colored quantities show significant correlation with the scatter in L_X at the low-mass end. This indicates that the systematic variation in the *kinetic* mode AGN feedback energy seen in Fig. 4 is not due to systematic variations in the SMBH mass, but rather intrinsic scatter in the accretion and assembly histories of those SMBHs. The middle and bottom panels of Fig. B1 suggest that the scatter in $L_{X,500}$ at the low-mass end is not significantly impacted by cumulative or recent radiative mode AGN feedback, consistent with the scenario that radiative mode AGN feedback is subdominant compared to the kinetic mode in the SMBHs of $z = 0$ galaxies with $M_* \gtrsim 10^{11} M_{\odot}$ in IllustrisTNG (Zinger et al. 2020). Since radiative mode AGN feedback is mostly shut off for most of these ETGs below $z = 0.1$ (bottom panel), it is unlikely to be an effective heat source that could alter L_X and affect the scatter in the scaling relation.

APPENDIX C: SPECTROSCOPIC-LIKE VERSUS MASS-WEIGHTED TEMPERATURES

In Fig. C1 we show the temperature comparison between the spectroscopic-like ($T_{\text{sl},500}$) definition and mass-weighted definition ($T_{\text{mw},500}$). The definition of $T_{\text{sl},500}$ follows from Equation 1 and the definition of ($T_{\text{mw},500}$) follows from Equation 2. The $T^{-3/4}$ weighting for $T_{\text{sl},500}$ makes the $T_{\text{mw},500}$ of the simulated ETGs ~ 0.2 dex higher than their $T_{\text{sl},500}$.

This paper has been typeset from a \LaTeX file prepared by the author.

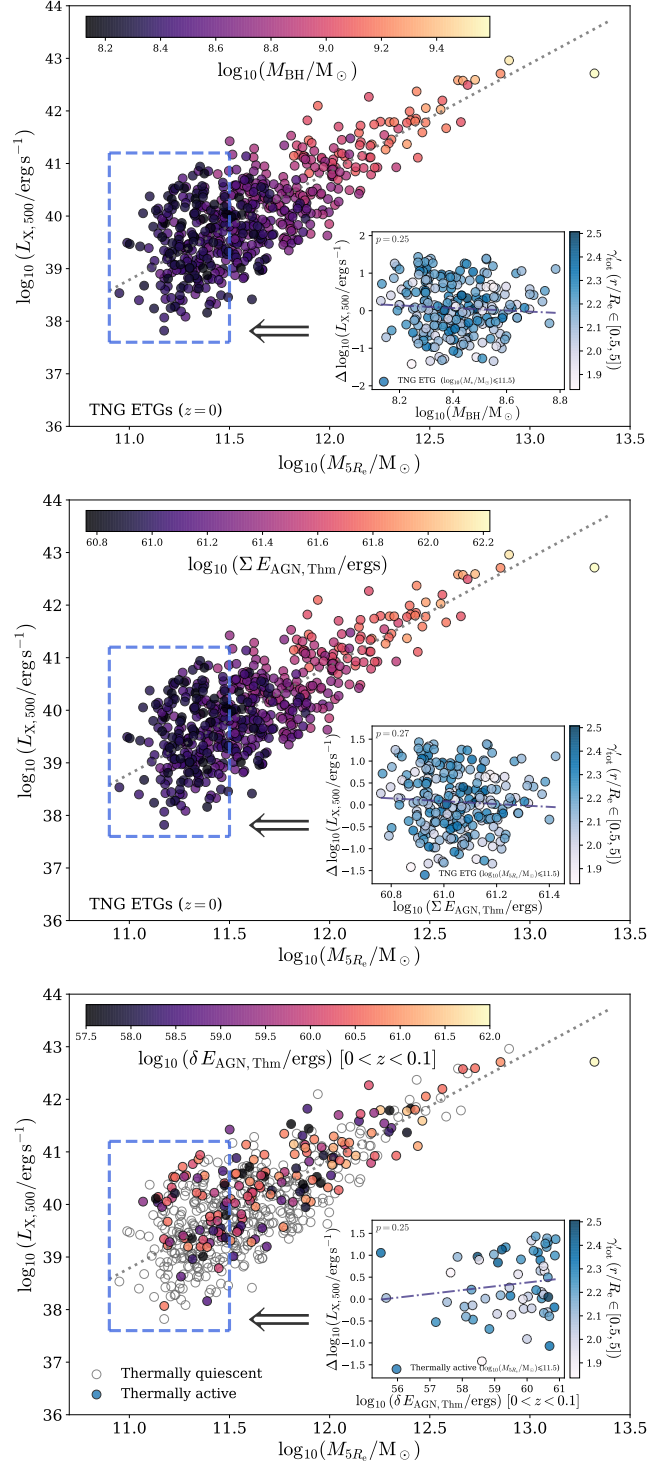


Figure B1. Similar to Fig. 4, we show the $L_{X,500}$ – M_{5R_e} scaling relation colored by the central SMBH mass (M_{BH} , top panel), cumulative radiative (thermal) mode AGN feedback energy ($\Sigma E_{\text{AGN,Thm}}$, middle panel), and recent thermal AGN feedback energy within $0 < z < 0.1$ ($\delta E_{\text{AGN,Thm}}$, bottom panel). In the bottom panel, quiescent SMBHs that did not emit any thermal energy at $z < 0.1$ are denoted with empty circles. The inset plots in each panel shows $\Delta L_{X,500}$ versus the respective colored black hole property in the main scaling relation for low-mass ETGs (blue dashed box, $\log_{10}(M_{5R_e}/M_{\odot}) \leq 11.5$). The lack of color gradient in the blue boxes and large Pearson p values for the linear fits in the insets indicate insignificant correlation of $L_{X,500}$ with all three black hole properties shown in the color scale.

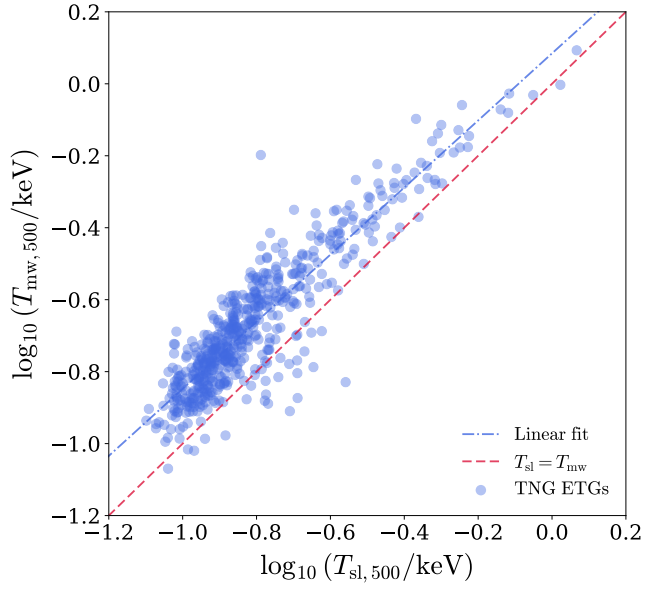


Figure C1. The spectroscopic-like temperature ($T_{\text{sl},500}$) versus the mass-weighted temperature ($T_{\text{mw},500}$) for our simulated ETGs (blue dots). The red dashed line stands for $T_{\text{sl},500} = T_{\text{mw},500}$, while the blue dotted-dashed curve is the linear fit to the log temperatures. According to the linear fit, $\log_{10} T_{\text{mw},500}$ is mostly higher than $\log_{10} T_{\text{sl},500}$ by ~ 0.2 dex.